Research Square

Preprints are preliminary reports that have not undergone peer review.
They should not be considered conclusive, used to inform clinical practice,
or referenced by the media as validated information.

Connecting the Drops: Computational Dissection of Intrinsic Disorder and Phase-Separation Propensity in the U2OS Tunneling Nanotube Proteome

Mohamed A. Khalaf
University of South Florida
Arjan van der Vaart
University of South Florida
Vladimir N. Uversky
vuversky@usf.edu

University of South Florida

Article

Keywords: tunneling nanotubes, intrinsically disordered proteins, liquid–liquid phase separation, FuzDrop, CH-CDF, protein–protein interaction network, short linear motifs, CD9, CD81, osteosarcoma

Posted Date: November 16th, 2026

DOI: https://doi.org/10.21203/rs.3.rs-11420044/v1

License: This work is licensed under a Creative Commons Attribution 4.0 International License.
Read Full License

Additional Declarations: No competing interests reported.

Connecting the Drops: Computational Dissection of Intrinsic Disorder and Phase-Separation Propensity in the U2OS Tunneling Nanotube Proteome

Mohamed A. Khalaf,[1] Arjan van der Vaart,[1] and Vladimir N. Uversky [2,3,*]

[1] *Department of Chemistry, University of South Florida, 4202 E Fowler Ave, CHE 205, Tampa, FL, 33620, USA; mohamedmahmoud@usf.edu (M.A.K.); avandervaart@usf.edu (A.v.d.V.)*

[2] *Department of Molecular Medicine, Morsani College of Medicine, University of South Florida, Tampa, FL 33612, USA*

[3] *USF Health Byrd Alzheimer's Research Institute, Morsani College of Medicine, University of South Florida, Tampa, FL 33612, USA*

*** Correspondence**: vuversky@usf.edu

Abstract: Tunneling nanotubes (TNTs) are actin-supported open membrane conduits that connect remote cells and carry vesicles, organelles, RNAs, and protein aggregates. A recent proteomic study defined the TNT proteome (TNTome) of U2OS human osteosarcoma cells as a set of 1,177 proteins and identified the tetraspanins CD9 and CD81 as non-redundant TNT regulators. Here we performed a proteome-wide computational analysis of the intrinsic disorder and liquid–liquid phase-separation (LLPS) propensity of the TNTome using RIDAO, CH-CDF analysis, D^2P^2, FuzDrop, the ELM resource, STRING, AlphaFold, and AFflecto. Of 1,176 proteins with complete predictions, 255 (21.7%) were highly disordered and 443 (37.7%) mostly ordered, with a mean disorder of 27.6 ± 27.2%. Among 253 highly disordered proteins scored by FuzDrop, 219 (86.6%) were predicted LLPS drivers; these drivers formed a dense STRING network (209 proteins, 2,200 edges, 21 hubs led by HNRNPA1, HNRNPC, HNRNPA2B1, SRSF1, NPM1, and FUS) that was strongly enriched in RNA-binding, mRNA-processing and ribonucleoprotein-complex functions. A bilateral deep dive into the 15 most disordered and 15 most ordered proteins, together with a catalogue of 1,647 short linear motifs, suggested a two-tier architecture, in which disordered, phase-separation-competent scaffolds coexist with ordered structural and enzymatic modules, including CD9 and CD81. We emphasize that all disorder predispositions and LLPS assignments are predictive and that, because the TNTome is cancer-derived and no non-cancer TNT proteome exists, the disorder/LLPS enrichment cannot yet be ascribed to TNT biology versus the malignant state. These intrinsically disordered proteins (IDPs) and intrinsically disordered regions (IDRs) and their predicted condensate behavior represent testable hypotheses for the molecular organization of TNTs.

Keywords: tunneling nanotubes; intrinsically disordered proteins; liquid–liquid phase separation; FuzDrop; CH-CDF; protein–protein interaction network; short linear motifs; CD9; CD81; osteosarcoma

Abbreviations

ACAT1	acetyl-CoA acetyltransferase 1
AKAP12	A-kinase anchor protein 12
ALYREF	Aly/REF export factor (THO complex subunit 4)
CD9	cluster of differentiation 9
CD63	cluster of differentiation 63
CD81	cluster of differentiation 81
CD151	cluster of differentiation 151
CCDC124	coiled-coil domain containing 124
CDF	cumulative-distribution-function
CDV3	carnitine deficiency-associated gene expressed in ventricle 3
CH	charge–hydropathy
D^2P^2	database of disordered protein predictions
DOC	docking
ELM	eukaryotic liner motif
ESD	esterase D
FDR	false-discovery-rate
FUS	fused in sarcoma
FuzDrop	fuzzy droplets
G3BP1	Ras GTPase-activating protein-binding protein 1 GAP SH3 domain-binding protein 1
GGH	gamma-glutamyl hydrolase
GLRX	glutaredoxin-1
GO	Gene Ontology
HMGB2	high-mobility-group box 2 protein
HNRNPA1	heterogeneous nuclear ribonucleoprotein A1
HNRNPA2B1	heterogeneous nuclear ribonucleoproteins A2/B1
HNRNPC	heterogeneous nuclear ribonucleoproteins C1/C2
HNRNPD	heterogeneous nuclear ribonucleoprotein D0
HNRNPDL	heterogeneous nuclear ribonucleoprotein D-like
HNRNPM	heterogeneous nuclear ribonucleoprotein M
HNRNPU	heterogeneous nuclear ribonucleoprotein U
IDR	intrinsically disordered region
IDP	intrinsically disordered protein
ILF3	interleukin enhancer-binding factor 3
JPT1	Jupiter-family microtubule-associated protein 1
JPT1	Jupiter-family microtubule-associated protein 1
KEGG	Kyoto encyclopedia of genes and genomes
KHDRBS1	KH domain-containing, RNA-binding, signal transduction-associated protein 1
LIG	ligand-binding
LLPS	liquid–liquid phase-separation
MARCKS	myristoylated alanine-rich C-kinase substrate
MARCKSL1	MARCKS-related protein
MOD	post-translational modification

MYH10	myosin-10
NPC2	Niemann-Pick disease type C2 protein (NPC intracellular cholesterol transporter 2)
NPM1	nucleophosmin
PHB1	prohibitin-1
PHGDH	D-3-phosphoglycerate dehydrogenase
PIP	prolactin-inducible protein
p_{LDDT}	predicted local distance difference test (ranges from 0 to 100), a measure of the per-residue confidence in AlphaFold model
p_{LLPS}	probability of liquid-liquid phase separation in FuzDrop
PLOD2	procollagen-lysine,2-oxoglutarate 5-dioxygenase 2
PPI	protein–protein interaction
PPIDR	predicted intrinsically disordered residues
PPT1	palmitoyl-protein thioesterase 1
PRDX5	peroxiredoxin-5
PTMA	prothymosin α
PTMS	parathymosin
RBMX	RNA-binding motif protein, X chromosome
RIDAO	rapid intrinsic disorder analysis online
RMSF	root-mean-square fluctuation
RPL29	ribosomal protein eL29
SFPQ	splicing factor, proline- and glutamine-rich
SLiM	short linear motif
SMPDL3B	acid sphingomyelinase-like phosphodiesterase 3b
SNRNP70	U1 small nuclear ribonucleoprotein 70 kDa
SRSF1	serine/arginine-rich splicing factor 1
SRSF2	serine/arginine-rich splicing factor 2
SRSF3	serine/arginine-rich splicing factor 3
STMN1	stathmin
STRING	search tool for the retrieval of interacting genes/proteins
TMSB4X	thymosin β-4
TMSB10	thymosin β-10
TNT	tunneling nanotube
TNTome	TNT proteome
TPM1	tropomyosin-1
TPM2	tropomyosin-2
TRG	targeting
U2OS	Uppsala 2 osteosarcoma
UBE2K	ubiquitin-conjugating enzyme E2 K
UBL5	ubiquitin-like protein 5
YBX1	Y-box-binding protein 1

1. Introduction

Tunneling nanotubes (TNTs) are thin (ranging from 50 to 700 nanometers in diameter), F-actin-supported membranous channels that establish open cytoplasmic continuity between cells

separated by distances ranging from a few to more than one hundred micrometers, thereby providing a direct route for the intercellular transfer of vesicles, organelles, nucleic acids and even misfolded protein aggregates [1,2]. First described as nanotubular highways for organelle transport [1], TNTs and TNT-like connections are now recognized across diverse cell types, including immune cells [3], retinal photoreceptors [4], cardiac cells [5], and neural cells, where they have been implicated in development and in the spread of neurodegenerative pathology [6]. This breadth has made the molecular composition and regulation of TNTs a question of broad cell-biological and biomedical interest.

Despite this interest, the proteome of TNTs remained poorly defined until recently, in part because TNTs are fragile and difficult to separate from extracellular vesicles and other protrusions. Notario Manzano and colleagues addressed this gap by establishing a biochemical protocol to isolate TNTs from U2OS human osteosarcoma cells, yielding a TNT proteome (hereafter the TNTome) of 1,177 proteins, and by demonstrating experimentally that the tetraspanins CD9 and CD81 act as non-redundant regulators, CD9 stabilizing TNTs and CD81 being required for the functional transfer of cargo [2]. That study noted, in particular, that the TNTome is unexpectedly rich in ribonucleoproteins and translation-related factors, a feature whose structural and functional implications have not been explored.

A large body of work now establishes that intrinsically disordered proteins (IDPs) and intrinsically disordered regions (IDRs), rather than being non-functional, frequently underpin regulatory and scaffolding roles, often through short linear motifs and multivalent interactions [7]. Multivalency among disordered, low-complexity and prion-like sequences is a sufficient driver of liquid–liquid phase separation (LLPS), the process by which cells assemble membraneless biomolecular condensates that organize biochemistry in space and time [8-11]. Because many of the ribonucleoproteins enriched in the TNTome are canonical condensate-forming proteins, the TNTome is an attractive substrate for a disorder- and LLPS-centered analysis.

Here, we apply an established computational pipeline for intrinsic-disorder and phase-separation analysis, previously used to dissect virus–host and other proteomes and protein datasets, to the complete TNTome. We (i) classify all 1,177 proteins by disorder level using a four-group refinement of the conventional scheme; (ii) identify, with FuzDrop, the subset of highly disordered proteins predicted to drive LLPS; (iii) map the predicted-driver protein–protein interaction network and its functional enrichment with STRING; (iv) catalogue short linear motifs with the ELM resource; and (v) perform a bilateral deep dive into the 15 most disordered and the 15 most ordered proteins, anchored where possible by AlphaFold models and the primary literature. Throughout, we treat all phase-separation assignments as predictions and discuss them as hypotheses, and we are explicit about two important caveats: the TNTome derives from a cancer cell line and has no non-cancer counterpart for comparison.

Three aspects merit brief emphasis. First, the tetraspanins CD9 and CD81 do not act alone but nucleate dynamic membrane platforms termed tetraspanin-enriched microdomains, which cluster partner receptors and membrane-remodeling factors and underlie many protrusion- and fusion-

related processes; their prominence in the TNTome frames the question of how such ordered membrane organizers cooperate with the disordered cytosolic proteins that dominate this study [2]. Second, TNTs are increasingly implicated in disease: in cancer they transfer mitochondria and other cargo that promote chemoresistance and invasiveness, and in the nervous system they provide a conduit for the spread of pathological aggregates and contribute to neurodegeneration, so their molecular composition is of direct biomedical interest [6]. Third, systematic analyses of intrinsic disorder across functional proteomes have repeatedly shown that disordered, phase-separation-prone proteins are over-represented in regulatory and signaling machineries, motivating an analogous disorder-centered dissection of the intercellular-communication apparatus represented by the TNTome [7].

2. Materials and Methods

2.1. Protein Dataset

The TNTome protein set was obtained from the supplementary data of Notario Manzano et al. [2], comprising 1,177 proteins identified by mass spectrometry in purified TNT fractions from U2OS human osteosarcoma cells, together with their UniProt identifiers, protein names and iBAQ abundance values. Canonical amino-acid sequences (FASTA) were retrieved from UniProt and submitted to the bioinformatics platforms described below. One protein lacked complete per-residue disorder output and was excluded from disorder statistics, leaving 1,176 proteins for the global disorder analysis.

2.2. Intrinsic Disorder Analysis

Per-residue intrinsic-disorder propensity was computed with the Rapid Intrinsic Disorder Analysis Online (RIDAO) platform [12], which integrates the outputs of PONDR® VSL2, PONDR® VL3, PONDR® VLXT, PONDR® FIT, IUPred-Short and IUPred-Long. Residues with disorder scores ≥ 0.5 were considered disordered, and the percentage of predicted intrinsically disordered residues (PPIDR) was calculated for each protein. Following our previous practice but refining the conventional three-group scheme to better resolve the body of the distribution, proteins were classified into four groups by PPIDR: mostly ordered (PPIDR < 10%), partially disordered (10% ≤ PPIDR < 30%), moderately disordered (30% ≤ PPIDR < 50%), and highly disordered (PPIDR ≥ 50%). PONDR® VSL2 outputs were used for ranking, consistent with its validated accuracy and speed. The four-group classification is based on the RIDAO consensus disorder profile (per-residue score ≥ 0.5); PONDR® VSL2 was used additionally for ranking and, for cross-dataset comparisons involving externally reported PONDR® VSL2 values, as a common predictor. The membrane-protein reference set (n = 2,789; Human Protein Atlas "cellular membrane") was scored through the identical RIDAO pipeline.

2.3. CH-CDF Analysis

Binary classification of proteins by structural status was performed with the charge–hydropathy (CH) versus cumulative-distribution-function (CDF) approach [13,14]. The CH plot separates

disordered from ordered proteins on the basis of net charge and hydropathy, whereas the CDF analysis evaluates per-residue disorder scores against an order–disorder boundary. Each protein was assigned a distance from the CH boundary (dCH) and from the CDF boundary (dCDF); the resulting CH-CDF phase space partitions proteins into four quadrants: Q1 (disordered by both criteria), Q2 (CDF-disordered/CH-compact, "mixed"), Q3 (ordered by both), and Q4 (CH-disordered/CDF-ordered, "unusual").

2.4. Functional Disorder Annotation (D^2P^2)

To corroborate the RIDAO predictions and to annotate disorder-associated features, proteins were analyzed through the Database of Disordered Protein Predictions (D^2P^2) [15], which aggregates multiple disorder predictors and overlays molecular recognition features (MoRFs), post-translational-modification sites and SUPERFAMILY domains. Agreement between RIDAO and D^2P^2 disorder estimates was assessed for the proteins represented in both resources.

2.5. LLPS Propensity (FuzDrop)

The propensity of each highly disordered protein to undergo spontaneous LLPS was predicted with FuzDrop [16,17], which returns a probability of LLPS (p_{LLPS}) from the sequence and identifies droplet-promoting regions. Proteins with $p_{LLPS} \geq 0.60$ were classified as predicted LLPS drivers. Four proteins (PTMA, MARCKSL1, TMSB4X and TMSB10) initially failed to return a score. Two proteins that are not short, prothymosin α (PTMA, 111 residues) and MARCKS-related protein (MARCKSL1, 195 residues), initially failed to return a score; appending a single C-terminal glycine (a documented workaround for this FuzDrop parsing issue) resolved this, and both were scored as high-confidence LLPS drivers. The two genuinely short thymosins, thymosin β-4 and thymosin β-10 (TMSB4X and TMSB10, 44 residues each), fell below the length range over which FuzDrop is reliable and were not scored.

2.6. Short Linear Motifs (ELM)

Short linear motifs (SLiMs) were identified with the Eukaryotic Linear Motif (ELM) resource [18] for the 15 most disordered proteins. Motifs were tallied in total and by ELM class, ligand-binding (LIG), post-translational modification (MOD), targeting (TRG) and docking (DOC), and mapped onto the disordered regions of each protein.

2.7. Protein–Protein Interaction Network and Functional Enrichment

Protein–protein interaction (PPI) networks were constructed with the STRING database [19] for the predicted LLPS drivers, using *Homo sapiens* as the organism of protein origin and a minimum required interaction score of 0.400 (medium confidence; STRING v12.0). Network degree was computed for each node, and hub proteins were defined as the top decile by degree. Functional enrichment (Gene Ontology (GO) Biological Process, Molecular Function, and Cellular Component; KEGG (Kyoto Encyclopedia of Genes and Genomes) pathways [20,21]; and subcellular-compartment annotations) was obtained from STRING with Benjamini–Hochberg false-discovery-rate (FDR) correction; terms with FDR < 0.05 were considered significant.

Compartment enrichment of LLPS drivers relative to the full TNTome was tested with Fisher's exact test.

2.8. Three-Dimensional Structures

Predicted three-dimensional structures were retrieved from the AlphaFold Protein Structure Database [22] to illustrate the structural organization (or lack thereof) of selected proteins at the disorder extremes. In addition, conformational ensembles of the 15 most ordered proteins were generated from their AlphaFold models with the AFflecto web server [23], which identifies flexible regions (tails, linkers and loops) and samples them to produce physically plausible conformers; for each ensemble the per-conformation radius of gyration and the per-residue C_α root-mean-square fluctuation (RMSF, after Kabsch superposition) were computed from C_α coordinates.

2.9. Statistical Analysis

Associations were quantified with Pearson and Spearman correlation coefficients, group comparisons with the Kruskal–Wallis and Mann–Whitney U tests, and categorical enrichments with Fisher's exact test, as appropriate. Two-sided p-values are reported, and FDR correction was applied to enrichment analyses. Percentages for the four disorder classes are expressed relative to the 1,176 proteins with complete disorder data.

3. Results

3.1. Global Intrinsic-Disorder Landscape of the TNTome

To characterize the structural organization of the TNTome, we computed per-residue disorder for all 1,177 proteins; 1,176 returned complete profiles and were classified into four groups by PPIDR (Table 1). The TNTome spanned the full disorder spectrum: 443 proteins (37.7%) were mostly ordered, 304 (25.9%) partially disordered, 174 (14.8%) moderately disordered, and 255 (21.7%) highly disordered, with a mean disorder of 27.6 ± 27.2% and a median of 17.6% (interquartile range 4.5–45.8%) (Figure 1). Thus, although the modal protein is well structured, more than one-fifth of the TNTome is highly disordered, a substantial disordered fraction for a membrane- and cytoskeleton-associated proteome. To test whether this disorder profile is specific to the TNTome or merely reflects its membrane-associated composition, we classified, through the identical RIDAO pipeline, a reference set of human plasma-membrane proteins (Human Protein Atlas "cellular membrane" annotation; n = 2,789 [24]) and compared both to published whole-proteome PONDR® VSL2 values (20,317 proteins [25]).

Table 1. Four-group intrinsic-disorder classification of the TNTome. Proteins were classified by the percentage of predicted intrinsically disordered residues (PPIDR); percentages are relative to the 1,176 proteins with complete disorder predictions.

Disorder class (PPIDR)	Number	Percent	Color
Mostly ordered (<10%)	443	37.7%	blue
Partially disordered (10–30%)	304	25.9%	violet
Moderately disordered (30–50%)	174	14.8%	pink
Highly disordered (≥50%)	255	21.7%	red

Total	**1,176**	**100%**	

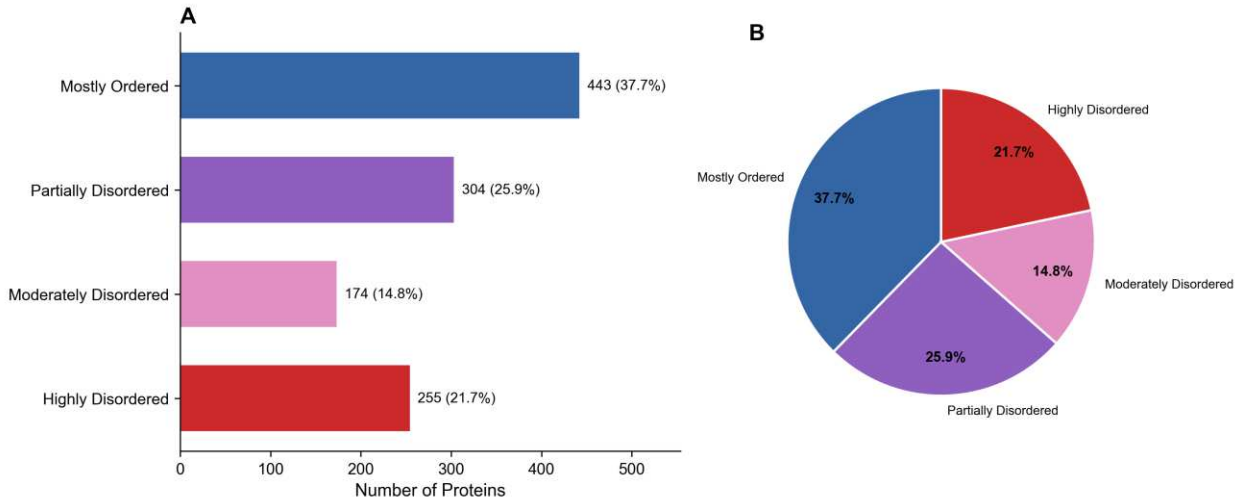


Figure 1. Distribution of intrinsic-disorder classes across the TNTome. (A) Number of proteins in each of the four PPIDR-based disorder classes; (B) the same data as proportions of the 1,176 proteins with complete disorder predictions. Mostly ordered proteins (37.7%) form the largest class, while highly disordered proteins constitute 21.7% of the proteome.

Because our four-group classification is based on the RIDAO consensus whereas the published proteome values are PONDR® VSL2, we performed the cross-set comparison on a single common predictor (PONDR® VSL2) in addition to our primary consensus classification. On the common PONDR® VSL2 metric, the highly disordered fraction was lowest for membrane proteins (26.5%), intermediate for the TNTome (32.8%) and highest for the whole proteome (37.4%); on our primary consensus metric the TNTome and membrane sets had almost identical mostly-ordered fractions (37.7% vs. 37.0%) but the TNTome carried a substantially larger highly-disordered tail (21.7% vs. 14.7%). By both predictors, the TNTome was significantly more disordered than the membrane-protein control (χ^2 four-group test, $p = 6.3 \times 10^{-4}$ for PONDR® VSL2 and $p = 1.3 \times 10^{-7}$ for the consensus; Figure 2). Thus, the substantial disordered fraction of the TNTome is not a trivial consequence of its membrane- and cytoskeleton-associated composition — membrane proteins are, if anything, more ordered — indicating that the disordered, phase-separation-prone tier is a genuine feature of this proteome rather than an artifact of subcellular localization.

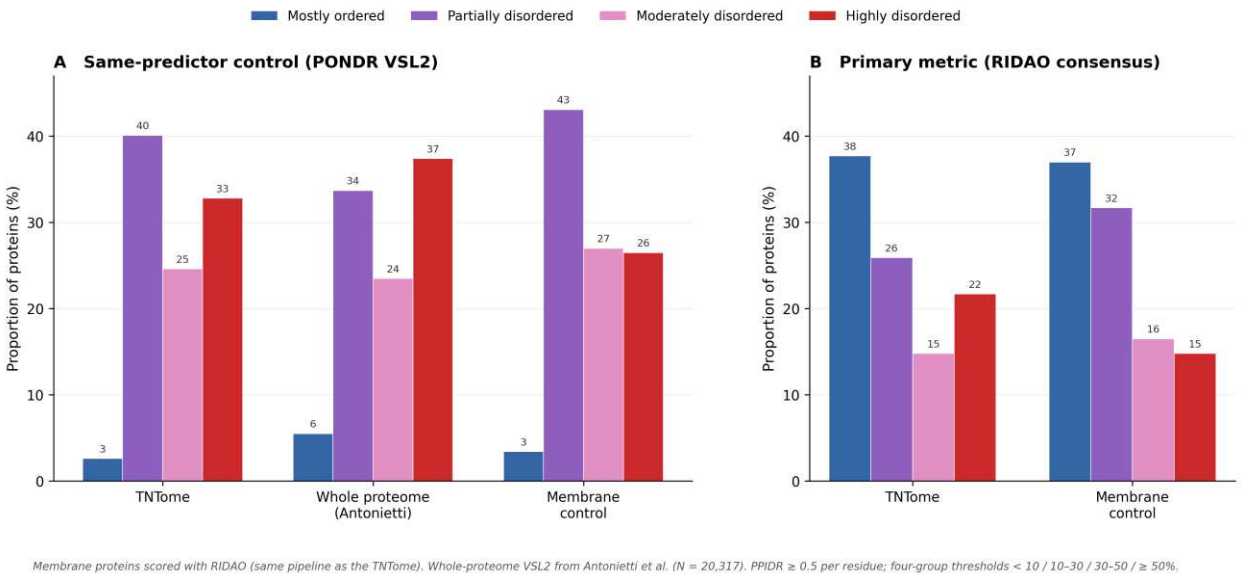


Figure 2. Intrinsic-disorder distribution of the TNTome versus a membrane-protein control and the whole human proteome. (A) Same-predictor comparison (PONDR VSL2): four-group classification of the TNTome, the whole human proteome (Antonietti et al. [25], N = 20,317) and the Human Protein Atlas cellular-membrane control (scored at PPIDR ≥ 0.5 per residue via RIDAO, the identical pipeline used for the TNTome). (B) The same comparison on the study's primary RIDAO consensus metric (the proteome baseline is available only as VSL2). By both predictors the TNTome is significantly more disordered than the membrane control (χ^2 four-group test, $p = 6.3 \times 10^{-4}$ and $p = 1.3 \times 10^{-7}$). Colors follow the four-group scheme: blue, mostly ordered; violet, partially disordered; pink, moderately disordered; red, highly disordered.

The continuous distribution of per-protein disorder (Figure 3) was right-skewed, with a dense population of well-ordered proteins and a long tail of highly disordered species extending to 100% predicted disorder. The CH-CDF phase analysis (Figure 4) partitioned the proteome into Q1 (disordered by both criteria; 241 proteins, 20.5%), Q2 (mixed; 253, 21.5%), Q3 (ordered by both; 651, 55.4%) and Q4 (unusual; 31, 2.6%), confirming that a coherent, sizeable disordered subpopulation coexists with a structured majority. RIDAO and D^2P^2 disorder estimates were strongly concordant for the 246 proteins represented in both resources (Pearson r = 0.83, $p = 1.4 \times 10^{-63}$; Spearman ρ = 0.84; mean absolute difference 6.8%; Figure 5), supporting the robustness of the disorder calls.

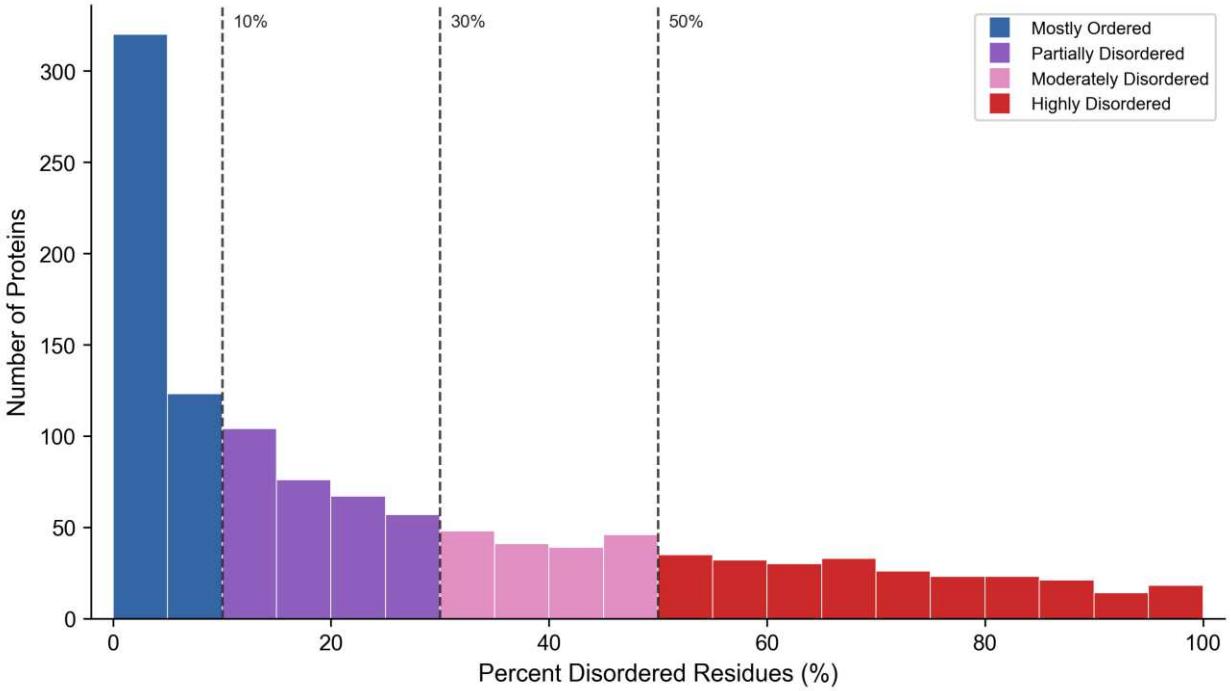


Figure 3. Distribution of predicted intrinsic disorder across the TNTome. Histogram of the percentage of predicted intrinsically disordered residues (PPIDR) for the 1,176 proteins with complete predictions. The distribution is right-skewed (median 17.6%, mean 27.6 ± 27.2%), with a long tail of highly disordered proteins.

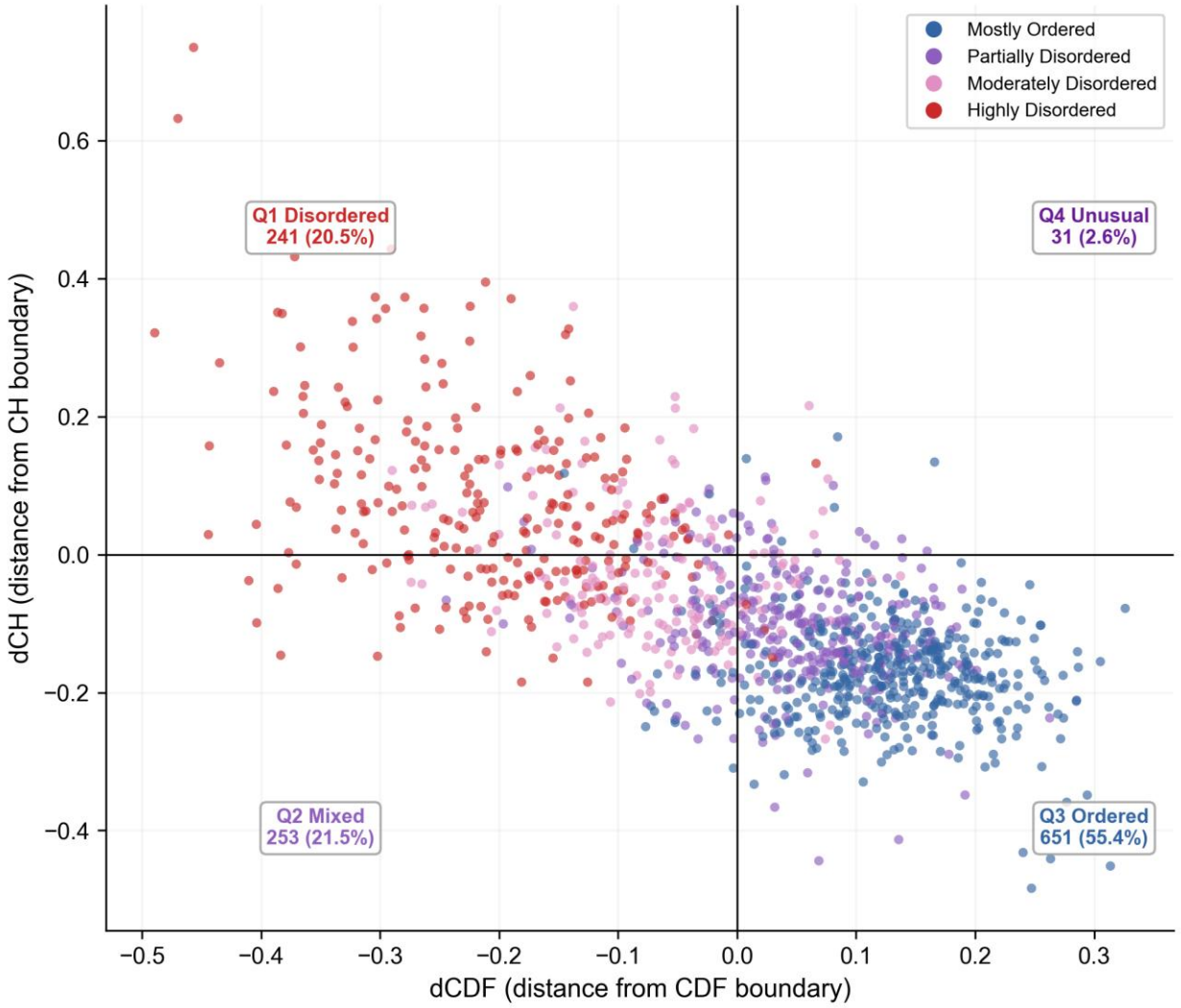


Figure 4. CH-CDF phase classification of the TNTome. Each protein is plotted by its distance from the CDF boundary (x-axis) and the CH boundary (y-axis) and colored by its four-group disorder class. Quadrants: Q1, disordered by both criteria (n = 241, 20.5%); Q2, mixed (n = 253, 21.5%); Q3, ordered by both (n = 651, 55.4%); Q4, unusual (n = 31, 2.6%).

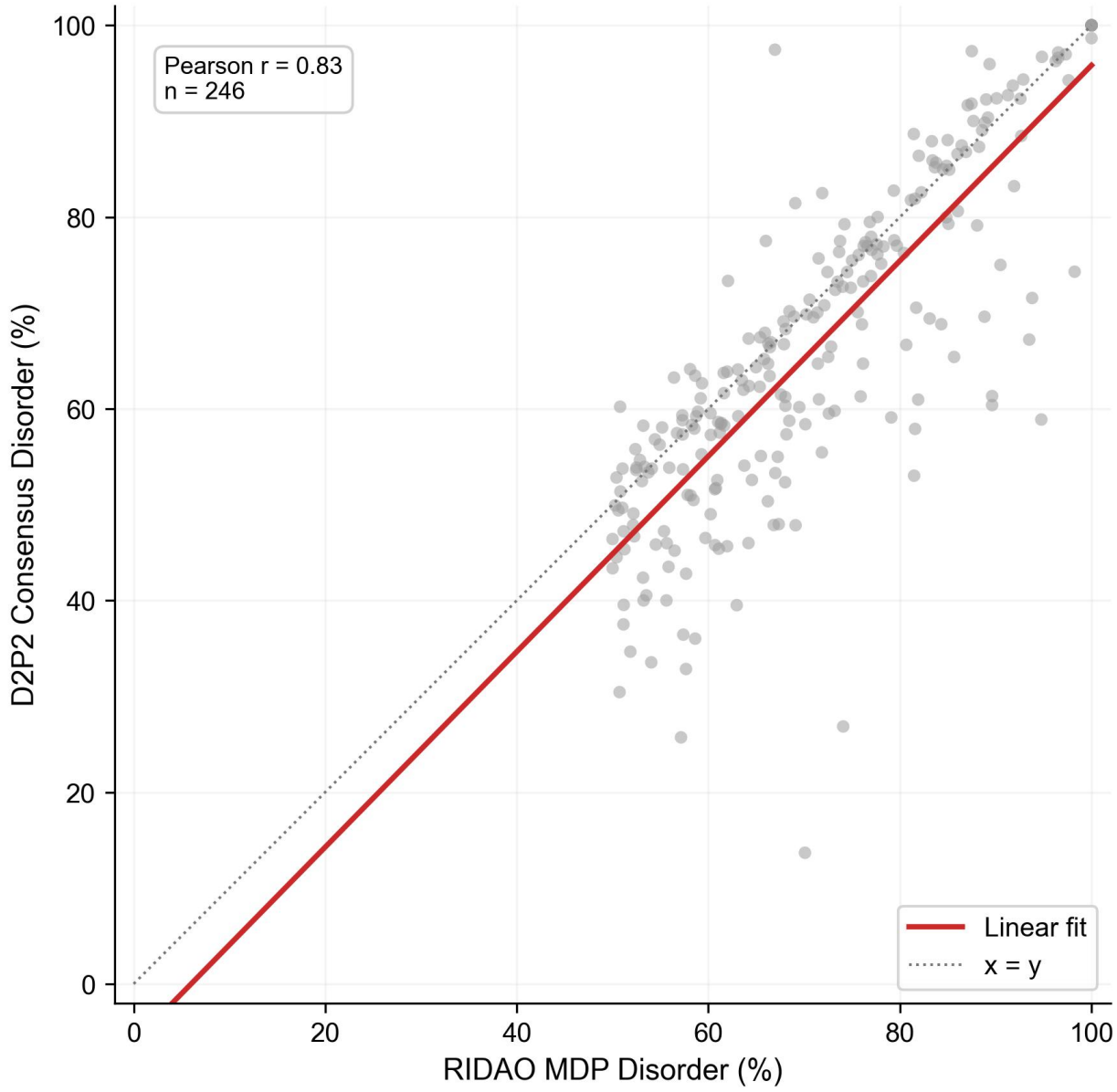


Figure 5. Concordance between RIDAO and D^{2}P^2 disorder predictions. Per-protein disorder estimates from RIDAO and D^{2}P^2 for the 246 proteins represented in both resources are strongly correlated (Pearson r = 0.83, $p = 1.4 \times 10^{-63}$; Spearman ρ = 0.84; mean absolute difference 6.8%).

3.2. The Disorder Extremes: A Bilateral Selection

To examine how disorder relates to function at the two ends of the spectrum, we selected the 15 most disordered and the 15 most ordered proteins of the TNTome for detailed analysis (Figure 6, Table 2). The 15 most disordered proteins were essentially fully disordered (PPIDR 97.3–100%) and included prothymosin α (PTMA), parathymosin (PTMS), thymosin β-4 and β-10 (TMSB4X, TMSB10), MARCKS-related protein (MARCKSL1), the Jupiter-family microtubule-associated

proteins JPT1 and JPT2, A-kinase anchor protein 12 (AKAP12), CCDC124, high-mobility-group protein HMGB2, stathmin (STMN1), ribosomal protein eL29 (RPL29) and CDV3. Two further proteins, tropomyosin-1 and tropomyosin-2 (TPM1, TPM2), were flagged as highly disordered by CH-CDF but are α-helical coiled-coils. However, because the coiled-coil fold of tropomyosins is stabilized only upon coiled-coil complex formation (binding-induced folding), their monomeric forms are predicted to be highly disordered, and they are therefore retained as bona fide highly disordered proteins in all analyses. The 15 most ordered proteins (PPIDR = 0%) were folded enzymes and structural modules, including the tetraspanin CD81, ACAT1, PHGDH, prohibitin-1 (PHB1), PPT1, NPC2, SMPDL3B, GGH, esterase D (ESD), peroxiredoxin-5 (PRDX5), glutaredoxin-1 (GLRX), UBL5, UBE2K, prolactin-inducible protein (PIP) and PLOD2; the second experimentally validated TNT regulator, CD9, was likewise predicted as near-fully ordered (2.2% disorder).

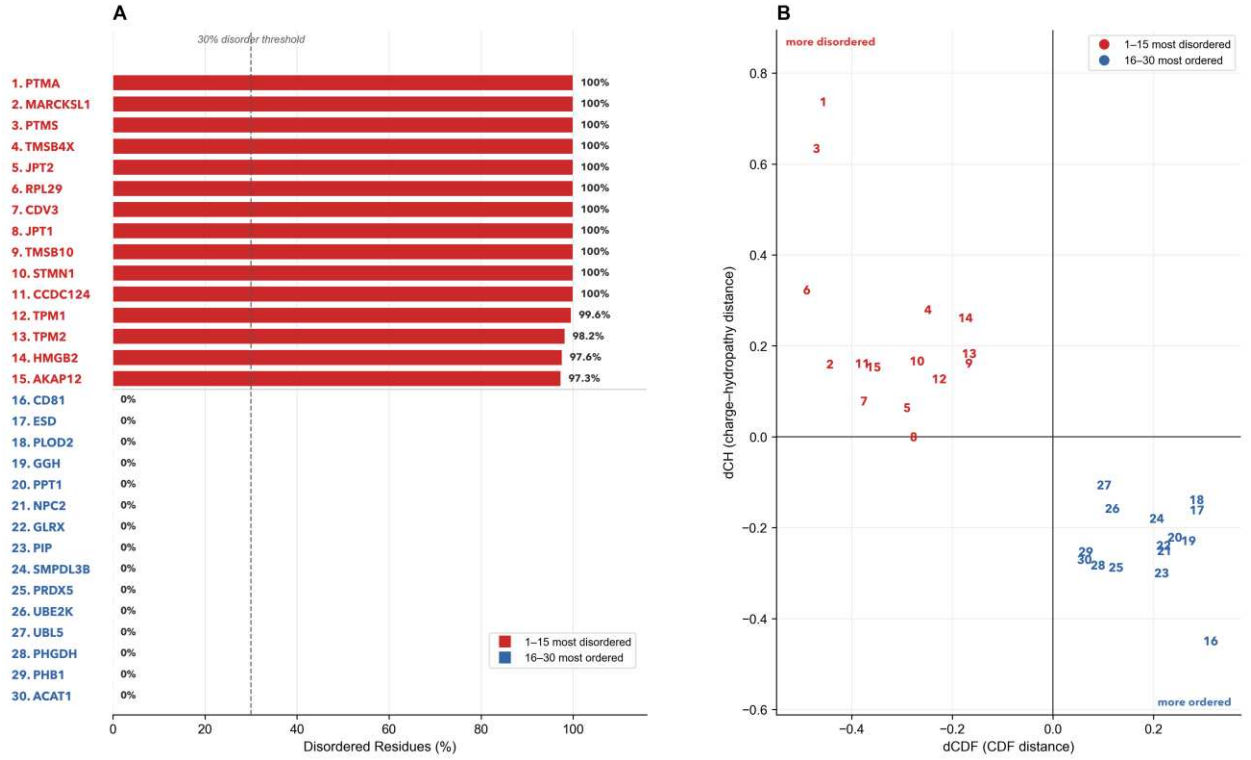


Figure 6. The intrinsic-disorder extremes of the TNTome. (A) Percentage of disordered residues for the 15 most disordered (red) and 15 most ordered (blue) proteins; the dashed line marks the 30% threshold and the numbers annotate the total ELM short-linear-motif count for each disordered protein. (B) Position of the same proteins within the CH-CDF phase space (all 1,176 proteins shown in grey); the most disordered proteins cluster in the highly disordered region (lower right) and the most ordered proteins in the mostly ordered region (upper left). TPM 1 and TPM2 are retained as highly disordered monomers.

Table 2. The 15 most disordered and 15 most ordered proteins of the TNTome. PPIDR, percentage of predicted intrinsically disordered residues; p_{LLPS}, FuzDrop probability of liquid–liquid phase separation (p_{LLPS} from FuzDrop; rescored with a C-terminal glycine extension for PTMA, and MARCKSL1, whereas TMSB4X, and TMSB10 not scored; ordered proteins not submitted); ELM, total short linear motifs. TPM1 and TPM2 are retained as highly disordered monomers. Ordered proteins all have PPIDR = 0% and were not scored for LLPS or motifs. (— = not analyzed; short-protein server timeout for TMSB4X, TMSB10.

Most disordered	PPIDR	p_{LLPS}	ELM	Most ordered	PPIDR
PTMA	100.0%	0.995	22	CD81	0.0%
MARCKSL1	100.0%	0.997	98	PIP	0.0%
PTMS	100.0%	0.995	30	GGH	0.0%
TMSB4X	100.0%	—	9	PLOD2	0.0%
JPT2	100.0%	0.995	60	ESD	0.0%
RPL29	100.0%	0.805	49	GLRX	0.0%
CDV3	100.0%	0.998	100	PPT1	0.0%
JPT1	100.0%	0.995	67	SMPDL3B	0.0%
AKAP12	97.3%	1.000	774	NPC2	0.0%
TMSB10	100.0%	—	10	UBL5	0.0%
STMN1	100.0%	0.860	53	PHB1	0.0%
CCDC124	100.0%	0.917	90	PHGDH	0.0%
HMGB2	97.6%	0.983	73	PRDX5	0.0%
TPM2 *	98.2%	0.713	110	ACAT1	0.0%
TPM1 *	99.6%	0.777	102	UBE2K	0.0%

3.3. LLPS Propensity across the TNTome

We next asked which highly disordered proteins are predicted to drive LLPS. Of the 255 highly disordered proteins, 253 returned FuzDrop scores (PTMA and MARCKSL1, which are not short, were rescored after appending a single C-terminal glycine; the two genuinely short thymosins TMSB4X and TMSB10 remained below FuzDrop's reliable length range and were not scored), and 219 (86.6%) were predicted LLPS drivers ($p_{LLPS} \geq 0.60$); 34 (13.4%) were non-drivers (Figure 7). Drivers and non-drivers were cleanly separated by score (driver mean $p_{LLPS} = 0.95$, median 0.99; non-driver mean = 0.37, median 0.36). Across this highly disordered set, p_{LLPS} correlated positively, though modestly, with the degree of disorder (Spearman $\rho = 0.40$, $p = 6.5 \times 10^{-11}$; Figure 8) and with sequence length (Pearson $r = 0.28$, $p = 5.2 \times 10^{-6}$; Figure S2), and negatively with protein abundance (p_{LLPS} versus $\log_{10}$ iBAQ, Pearson $r = -0.34$, $p = 2.1 \times 10^{-8}$). Disorder itself was independent of abundance across the whole TNTome (Spearman $\rho = 0.005$, $p = 0.86$; Kruskal–Wallis across iBAQ quartiles $p = 0.62$; Figure S1), indicating that the disordered fraction is not a low-abundance artifact. A CH-CDF quadrant view colored by driver status (Figure S3) confirmed that predicted drivers concentrate in the disordered quadrants.

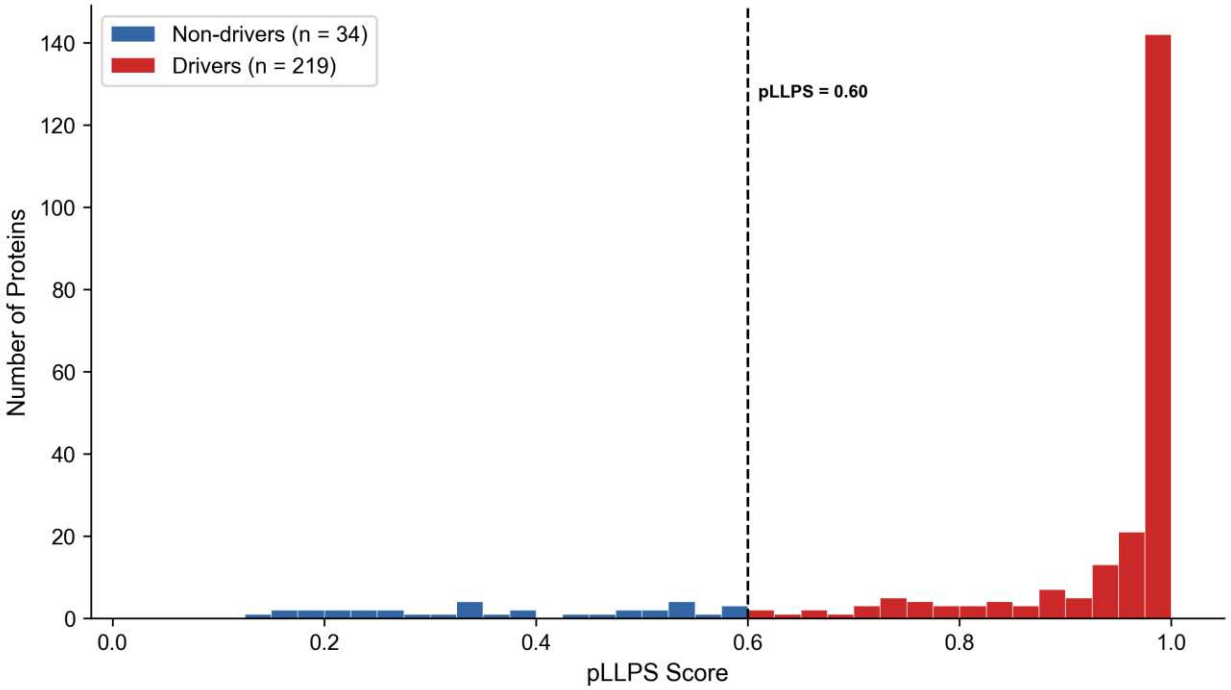


Figure 7. Distribution of FuzDrop LLPS propensity among highly disordered TNTome proteins. Histogram of p_{LLPS} scores for the 253 highly disordered proteins analyzed by FuzDrop (only PTMA and MARCKSL1 were rescued; the thymosins were not scored). Applying the $p_{LLPS} \geq 0.60$ threshold (dashed line), 219 proteins (86.6%) are predicted LLPS drivers and 34 (13.4%) are non-drivers.

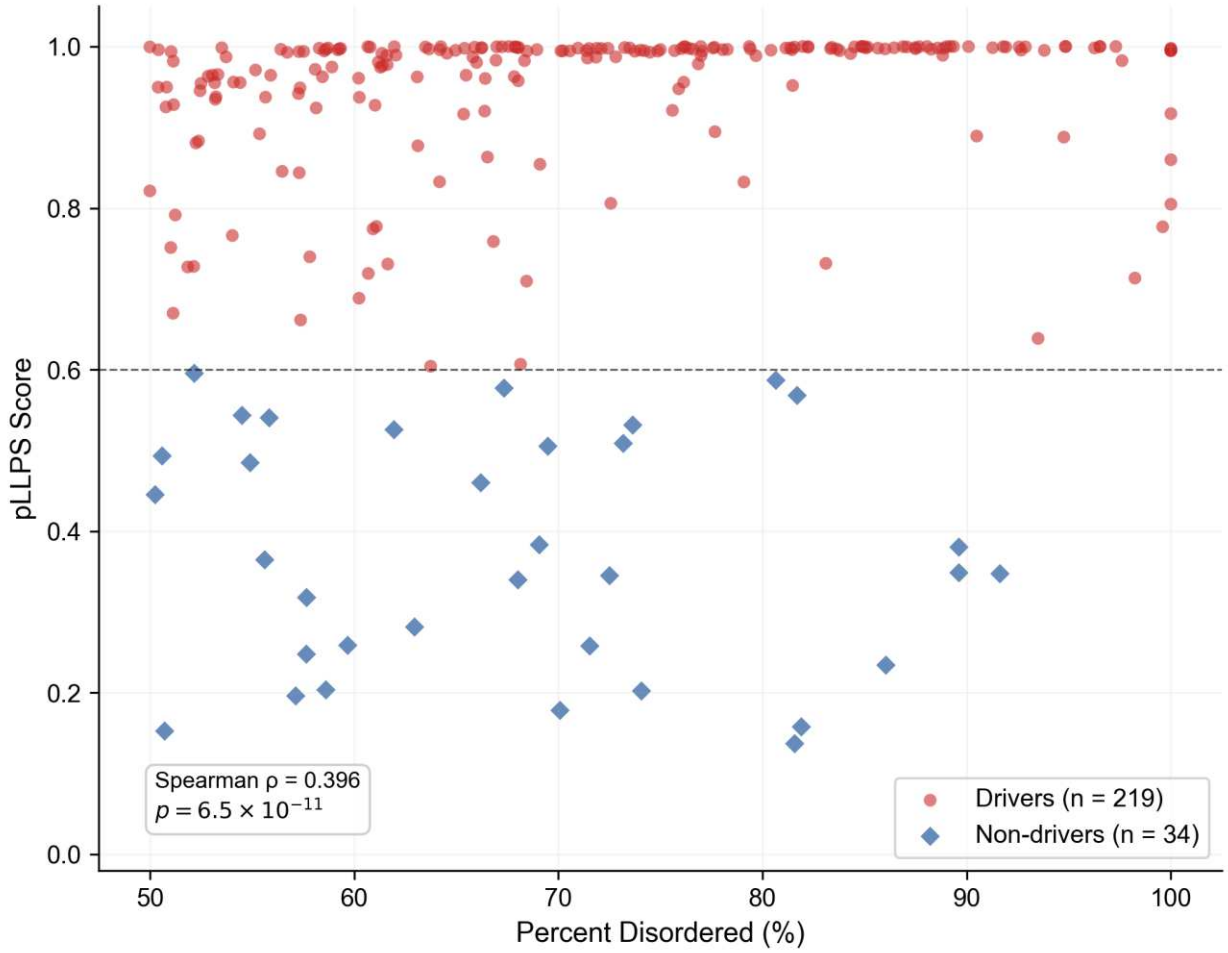


Figure 8. Relationship between LLPS propensity and intrinsic disorder. p_{LLPS} versus percentage of disordered residues for the highly disordered proteins, with predicted drivers (n = 219) and non-drivers (n = 34) indicated. The two variables are positively but modestly correlated (Spearman ρ = 0.40, $p = 6.5 \times 10^{-11}$), and nearly all proteins above the $p_{LLPS} = 0.60$ threshold are drivers.

3.4. Short Linear Motifs in the Most Disordered Proteins

Because disordered regions frequently act through short linear motifs, we catalogued ELM-defined motifs in the 15 most disordered proteins (Table 3). In total, 1,647 motif instances were identified, dominated by the modification (MOD) and ligand-binding (LIG) classes. The motif load was strikingly heterogeneous: AKAP12 alone carried 774 motifs, by far the most motif-dense protein in the dataset and consistent with its role as a multivalent signaling scaffold, followed by CDV3 (100), TPM2 (110), TPM1 (102), MARCKSL1 (98), CCDC124 (90) and HMGB2 (73). This dense, MOD/LIG-biased motif content is the molecular vocabulary through which these disordered proteins could engage many partners simultaneously, a property central to multivalency-driven condensate formation.

Table 3. Short linear motifs (ELM) in the 15 most disordered TNTome proteins. Motif counts by ELM class: LIG (ligand binding), MOD (post-translational modification), TRG (targeting), DOC (docking). TPM1 and TPM2 are included as highly disordered monomers (total across all 15 proteins, 1,647motifs).

Gene	UniProt	Total	LIG	MOD	TRG	DOC
PTMA	P06454	22	6	7	3	0
MARCKSL1	P49006	98	16	49	11	18
PTMS	P20962	30	9	7	4	3
TMSB4X	P62328	9	5	2	0	2
JPT2	Q9H910	60	26	14	1	14
RPL29	P47914	49	13	11	5	10
CDV3	Q9UKY7	100	42	33	2	13
JPT1	Q9UK76	67	23	28	2	9
AKAP12	Q02952	774	273	325	35	83
TMSB10	P63313	10	5	2	0	1
STMN1	P16949	53	13	21	2	7
CCDC124	Q96CT7	90	22	21	13	12
HMGB2	P26583	73	38	18	3	9
TPM1 *	H7BYY1	102	39	30	12	8
TPM2 *	Q5TCU3	110	45	32	10	10

3.5. Interaction Network and Functional Enrichment of the Predicted LLPS Drivers

Mapping the predicted LLPS drivers onto STRING yielded a dense, highly connected network of 209 proteins linked by 2,200 edges, with a mean degree of 21 (median 13, range 1–91) and 21 hub proteins in the top decile (Figure 9, Table 4). The hubs were overwhelmingly RNA-binding proteins, led by HNRNPA1 (degree 91), HNRNPC (79), HNRNPA2B1 (74), SRSF1 (72), SRSF3 (70), HNRNPM (66), NPM1 (66), HNRNPU (65) and FUS (64), proteins that are archetypal constituents of stress granules, the nucleolus, paraspeckles and nuclear speckles. Hubs had significantly higher degree than non-hubs (Mann–Whitney U, $p = 5.8 \times 10^{-14}$), but did not differ significantly in disorder (67.3% vs. 72.0%, $p = 0.18$) or p_{LLPS} (0.99 vs. 0.95, $p = 0.11$), indicating that connectivity, rather than disorder level per se, distinguishes the network core.

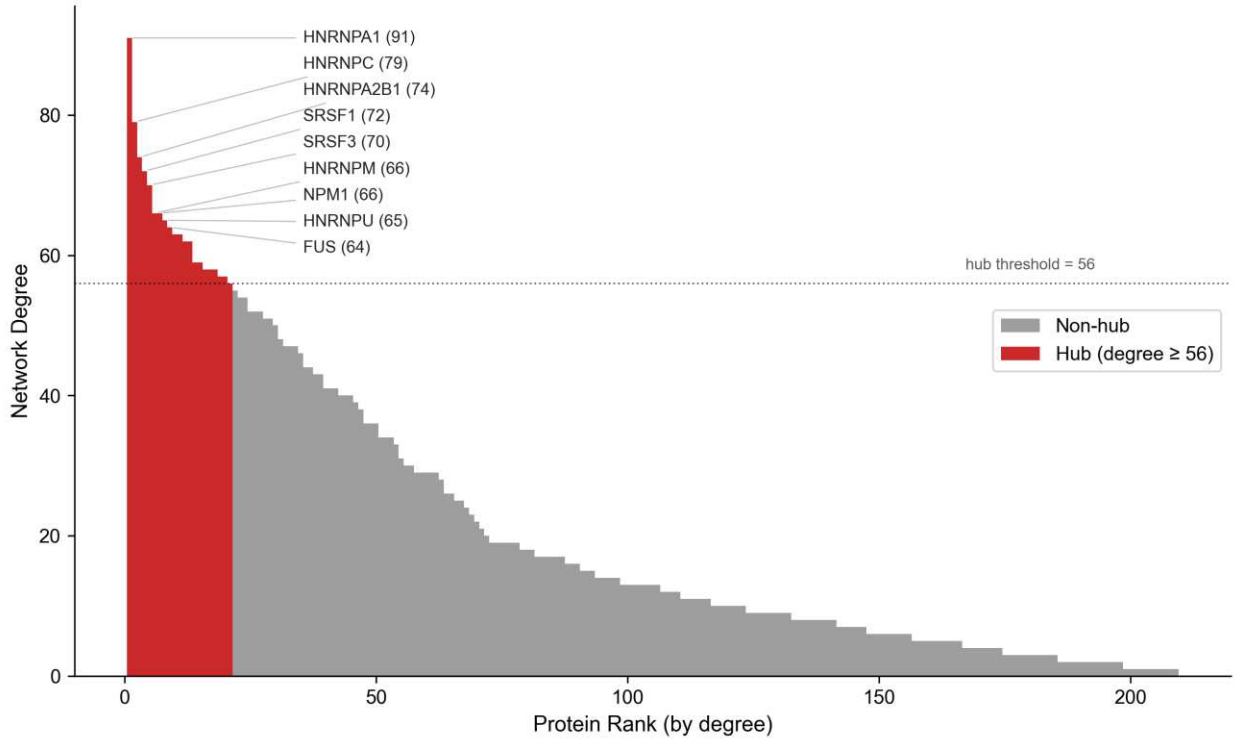


Figure 9. Connectivity of the predicted LLPS-driver interaction network. STRING network degree (number of interactions) for the 209 mapped LLPS drivers, ranked by degree. Hubs (top decile; degree ≥ 56) are highlighted and the most connected RNA-binding proteins are labeled; HNRNPA1 is the most connected node (degree 91).

Table 4. Hub proteins of the LLPS-driver interaction network. The 21 top-decile hubs (network degree ≥ 56) and their STRING degree.

Gene	Degree	Gene	Degree	Gene	Degree
HNRNPA1	91	HNRNPU	65	KHDRBS1	59
HNRNPC	79	FUS	64	HNRNPDL	58
HNRNPA2B1	74	RBMX	63	ILF3	58
SRSF1	72	YBX1	63	HNRNPD	58
SRSF3	70	ALYREF	62	SFPQ	57
NPM1	66	SRSF2	62	G3BP1	57
HNRNPM	57	SFPQ	56	SNRNP70	56

Functional-enrichment analysis of the driver network (Table 5, Figure 10) was dominated by RNA biology. The most significant Molecular Function term was RNA binding (126 genes, FDR = 4.9×10^{-71}), followed by nucleic-acid binding and mRNA binding; the top Biological Processes were mRNA processing, mRNA metabolism and RNA splicing; the leading Cellular Components were ribonucleoprotein complex, nucleus, nuclear lumen and spliceosomal complex; and the top KEGG pathway [20,21] was Spliceosome (FDR = 4.6×10^{-22}), with RNA transport and, notably, amyotrophic lateral sclerosis also enriched.

Table 5. Top functional-enrichment terms for the LLPS-driver network (STRING [19], FDR < 0.05). Representative top terms per category ranked by FDR; n = number of driver genes annotated to the term. KEGG pathway terms are from the KEGG database [20,21].

Category	Term	n	FDR
GO Process	mRNA processing	48	3.0×10^{-27}
GO Process	mRNA metabolic process	53	5.2×10^{-27}
GO Process	RNA splicing	41	3.5×10^{-24}
GO Function	RNA binding	126	4.9×10^{-71}
GO Function	Nucleic acid binding	138	2.0×10^{-39}
GO Function	mRNA binding	48	2.7×10^{-34}
GO Component	Ribonucleoprotein complex	55	3.7×10^{-27}
GO Component	Nucleus	158	9.0×10^{-21}
GO Component	Spliceosomal complex	28	6.2×10^{-19}
KEGG	Spliceosome	27	4.6×10^{-22}
KEGG	RNA transport	13	1.0×10^{-5}
KEGG	Amyotrophic lateral sclerosis	16	3.1×10^{-4}

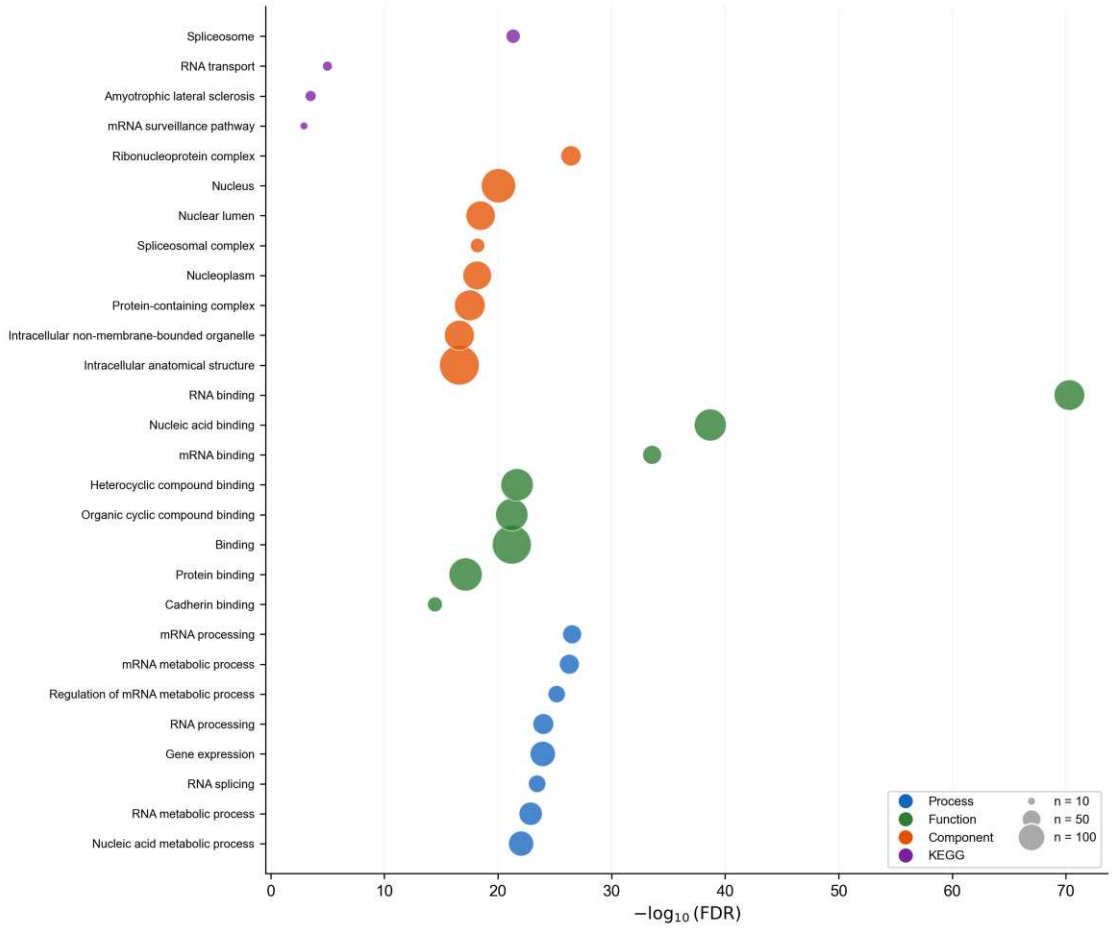


Figure 10. Functional enrichment of the LLPS-driver network. Dot plot of enriched Gene Ontology (Process, Function, Component) and KEGG pathway terms (STRING [19], FDR < 0.05). Dot size scales with the number of

driver genes annotated to each term and the x-axis shows $-\log_{10}$(FDR); RNA binding is the single most significant term. KEGG pathway annotations are from the KEGG database (Kanehisa Laboratories) [20,21].

Consistent with this, a compartment analysis (Figure 11) showed that LLPS drivers were significantly over-represented in the nuclear (58.0% vs. 48.3%; OR = 1.6, $p = 1.6 \times 10^{-3}$) and cytoskeletal (20.5% vs. 15.2%; OR = 1.6, $p = 2.1 \times 10^{-2}$) compartments, and significantly depleted from the exosomal (22.4% vs. 47.3%; OR = 0.26, $p = 5.0 \times 10^{-17}$), mitochondrial (2.3% vs. 13.0%; OR = 0.13, $p = 2.8 \times 10^{-9}$) and ribosomal (3.2% vs. 7.6%; OR = 0.35, $p = 4.5 \times 10^{-3}$) compartments; the membrane compartment did not differ significantly (49.3% vs. 55.2%; $p = 0.06$). Together, these analyses indicate that the predicted phase-separating core of the TNTome is a nuclear, ribonucleoprotein, splicing-associated module that is markedly under-represented among exosomal, mitochondrial and ribosomal proteins.

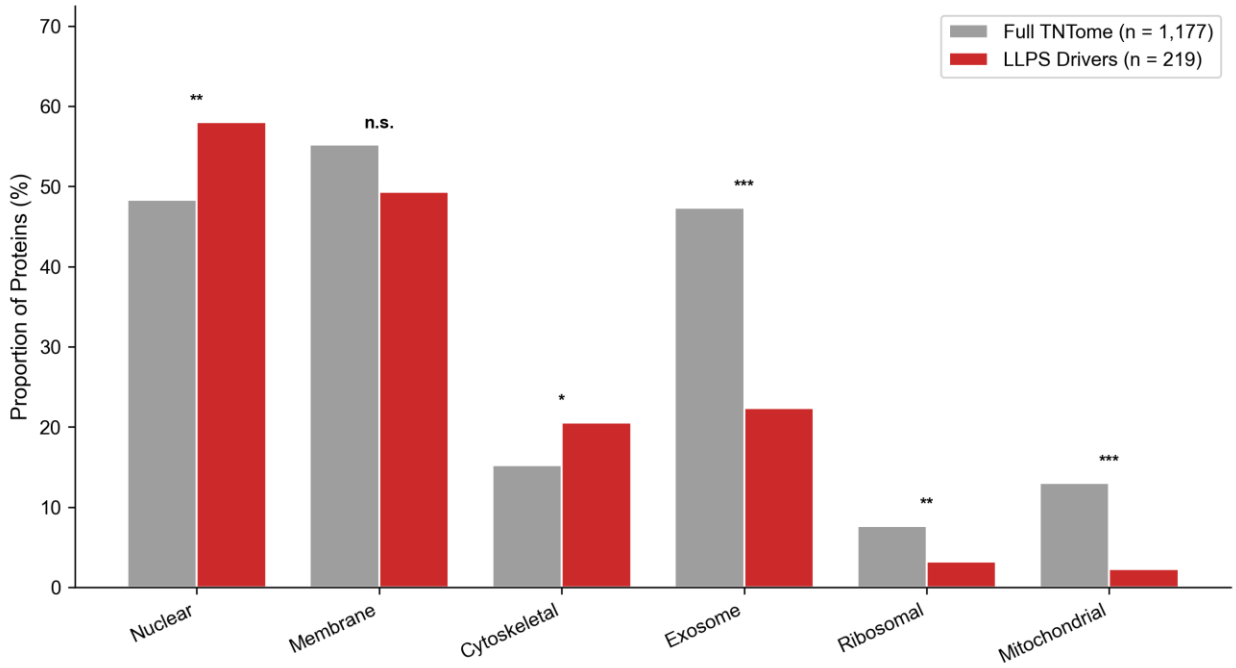


Figure 11. Subcellular-compartment distribution of LLPS drivers versus the full TNTome. Proportion of proteins annotated to each compartment for the full TNTome (n = 1,177) and the LLPS drivers (n = 219). Drivers are significantly enriched in the nuclear (**, $p = 1.6 \times 10^{-3}$) and cytoskeletal (*, $p = 2.1 \times 10^{-2}$) compartments and significantly depleted from the exosomal (***, $p = 5.0 \times 10^{-17}$), mitochondrial (***, $p = 2.8 \times 10^{-9}$) and ribosomal (**, $p = 4.5 \times 10^{-3}$) compartments (Fisher's exact test); the membrane compartment is not significant (n.s.).

Finally, we located the experimentally validated TNT regulators within this landscape. CD9 (2.2% disorder), CD81 (0%), and the related tetraspanins CD63 (1.3%) and CD151 (1.6%) were all mostly ordered and were not LLPS drivers, whereas among other functionally relevant TNT proteins the non-muscle myosin heavy chain MYH10 was highly disordered (56.5%) and a predicted driver ($p_{LLPS} = 0.85$). Thus the molecular machinery shown to build and gate TNTs is structured, while a large, separable disordered/phase-separation-competent module sits alongside it.

4. Discussion

Our proteome-wide analysis reveals that the TNTome is structurally bimodal: a well-folded majority coexists with a substantial, highly disordered minority that is overwhelmingly predicted to be phase-separation-competent and that assembles, in silico, into a tightly connected ribonucleoprotein network. We interpret these observations as a hypothesis of two-tier molecular organization, ordered structural and enzymatic modules (including the tetraspanins CD9 and CD81) operating alongside disordered, multivalent, motif-dense scaffolds with condensate potential. Below we discuss the functional logic of the disorder extremes, the special status of the RNA-binding network, the comparison between healthy and cancerous TNTs, and the evolutionary context of intercellular conduits. Two cautions frame the entire discussion: with a single exception, PTMA, for which a biomolecular condensate has now been experimentally characterized [26] (see Section 4.1), no direct experimental condensate evidence exists for TNTome proteins, so all other LLPS statements remain predictive.

4.1. Functional Intrinsic Disorder at the Disorder Extremes

The conceptual basis for a condensate-centered reading of the disordered tier is well established: multivalency among disordered, low-complexity and prion-like sequences is sufficient to drive intracellular phase separation [8]; native ribonucleoprotein bodies behave as liquid droplets [9]; a molecular grammar in which tyrosine and arginine residues encode the driving force has been defined [10]; and these phenomena are unified under the concept of biomolecular condensates as organizers of cellular biochemistry [11]. Against this backdrop, a proteome enriched in disordered, motif-dense proteins is a plausible, though not demonstrated, substrate for condensate-type organization.

For most of the 13 genuinely disordered extreme proteins, decades of biophysics show that disorder is mechanistically central rather than incidental. Prothymosin α is a canonical natively unfolded protein [27] whose disorder enables an ultrahigh-affinity yet fully disordered “fuzzy” complex with linker histone H1 [28] and competitive linker-histone exchange on nucleosomes [29]; its relative parathymosin similarly binds H1 and remodels chromatin [30]. The β-thymosins TMSB4X and TMSB10 fold only upon binding actin, which they sequester, a textbook case of disorder-enabled monomer sequestration [31]. MARCKSL1 acts through a disordered effector domain whose phosphorylation switches it into an F-actin bundler that drives filopodium dynamics [32] a behavior for which actin-regulator condensates such as those of VASP provide an independent precedent [33]. The Jupiter-family proteins JPT1 and JPT2 are disorder-prone microtubule- and signaling-associated proteins [34,35], with JPT2 additionally established as an essential NAADP-binding factor in calcium signaling [36]. AKAP12, the most motif-dense protein in the dataset, is a disordered multivalent scaffold that organizes PKA/PKC signaling [37], and biophysical work on disordered AKAP scaffolds shows how disorder generates hidden multivalency in partner recruitment [38]. CCDC124 bridges hibernating ribosomes and functions

at the centrosome/midbody [39,40]; HMGB2 is an architectural DNA-bending protein with a disordered acidic tail whose loss disrupts genome organization [41,42]; and stathmin is a textbook IDP that sequesters tubulin through folding-upon-binding [43-45]. eL29/RPL29 additionally moonlights as the cell-surface heparin/heparan-sulfate-binding protein HIP, whose expression is downregulated during differentiation [46]. By contrast, CDV3 remains essentially uncharacterized, with no experimental evidence that it is disordered beyond prediction; we flag it as the weakest-evidence case. Importantly, no experimental LLPS data exist for any of these specific proteins, and HMGB2 in particular should not be assigned LLPS, since condensate evidence in that family pertains to the paralog HMGB1; the literature cited establishes only the plausibility of the FuzDrop predictions. Since this analysis was completed, direct experimental evidence has emerged that prothymosin α forms a genuine biomolecular condensate: at single-molecule resolution it assembles a highly dynamic complex coacervate with linker histone H1 [26]. This is the first TNTome protein with experimentally demonstrated condensate behavior, although it reflects heterotypic coacervation with H1 rather than homotypic self-assembly, so the remaining disordered proteins stay predictive. CCDC124 is, moreover, condensate-adjacent rather than condensate-silent: it localizes to G3BP1-positive stress granules in U2OS cells and its disordered coiled-coil drives dimerization and aggregation in vitro [47,48]. MARCKSL1 is further supported as a membrane-cortex and mechanoresponse regulator that tunes cell shape and protrusive behavior [49], consistent with a role at membrane protrusions such as TNTs.

The opposite extreme comprises folded enzymes and structural modules whose functions depend on defined three-dimensional architecture, and it is here that the two validated TNT regulators reside. CD81 is the prototypic tetraspanin, with a defined extracellular-loop fold [50], a full-length structure enclosing a cholesterol-binding pocket [51], and a partner-scaffolding role illustrated by the CD19–CD81 complex [52]; in the source proteome it is specifically required for functional cargo transfer through TNTs [2]. CD9 shares the tetraspanin fold and a curvature-inducing shape that informs tetraspanin-enriched-microdomain assembly [53,54] and stabilizes TNTs [2]. The remaining ordered extremes are well-characterized enzymes, ACAT1 (thiolase) [55,56], PHGDH (serine synthesis) [57], the mitochondrial scaffold prohibitin-1 [58], PPT1 [59,60], the cholesterol carrier NPC2 [61-63], SMPDL3B [64,65], GGH [66], esterase D [67,68], peroxiredoxin-5 [69-71], glutaredoxin-1 [72,73], the splicing-associated ubiquitin-like protein UBL5 [74,75], the ubiquitin-conjugating enzyme UBE2K [76,77], the secreted glycoprotein PIP [78,79], and the collagen-modifying PLOD2, whose fold is inferred from its LH3 homolog and which is secreted to act extracellularly [80-82]. With the exception of CD9 and CD81, none of these has a reported TNT-specific role, although NPC2 (extracellular-vesicle cholesterol efflux) [63] and PRDX5 (extracellular release) [71] have transfer-adjacent functions; this asymmetry reinforces a model in which structured proteins supply defined activities while the disordered tier could provide dynamic organization. A recent biophysical finding reinforces the placement of the tetraspanins in this ordered, membrane-shaping tier: CD9 and TSPAN4 directly sense positive membrane curvature and are recruited to membrane tubes and protrusions [83], providing a physical basis for tetraspanin enrichment on TNTs.

This structural dichotomy is captured directly by the AlphaFold models of representative proteins from the two tiers (Figures 12 and 13). The most disordered proteins render as extended, largely low- to moderate-confidence chains, most dramatically AKAP12 (mean p_{LDDT} = 41), a sprawling multivalent scaffold (Figure 12). On the contrary, the most ordered proteins, including the TNT regulator CD81, form compact, high-confidence globular folds (Figure 13). AlphaFold models of all 15 most disordered and all 15 most ordered proteins are provided as Figures S4 and S5.

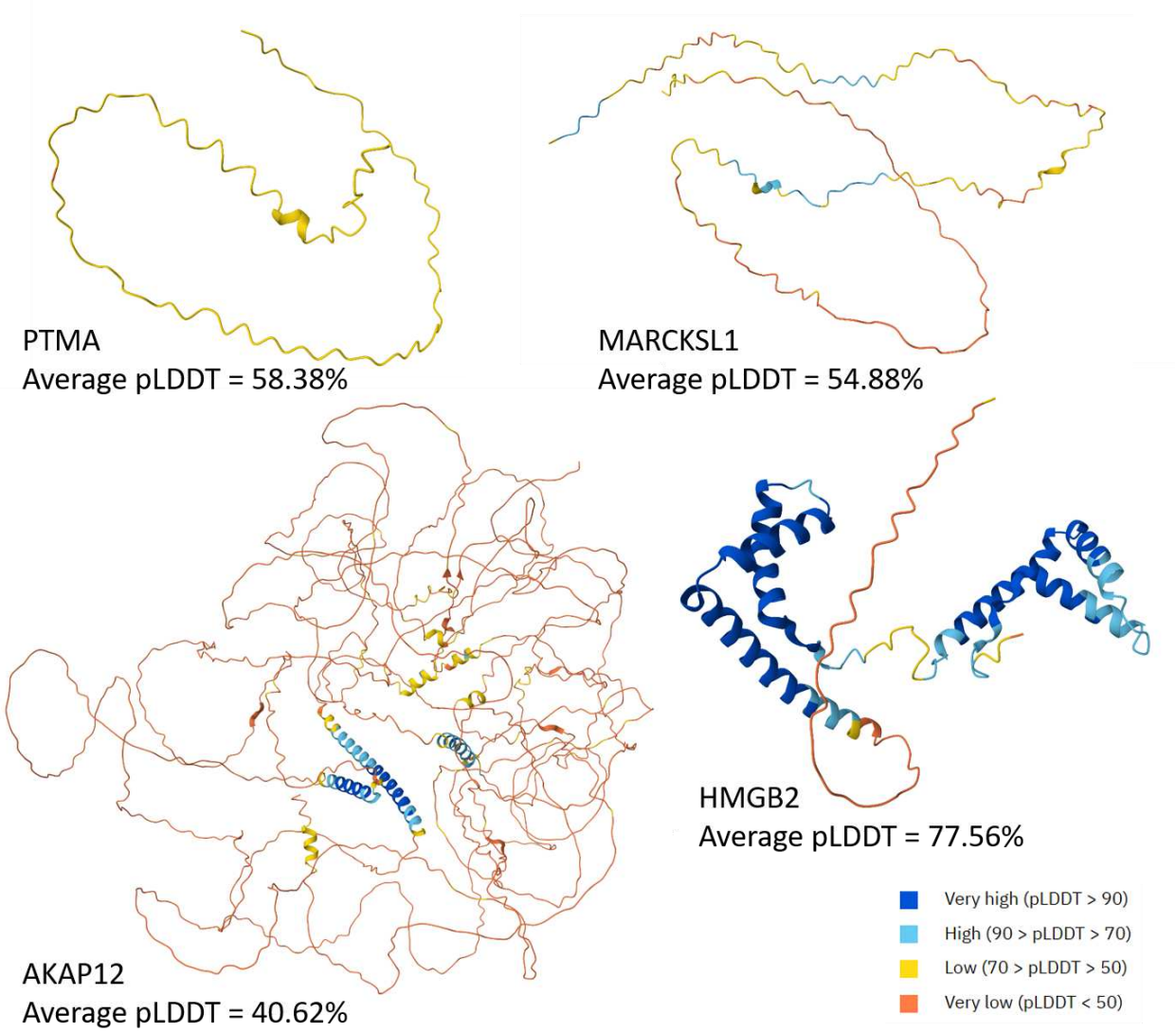


Figure 12. AlphaFold models of representative TNTome proteins at the disorder extremes, colored by per-residue confidence (p_{LDDT}). Four of the most disordered proteins (PTMA (UniProt ID: P06454), MARCKSL1 (UniProt ID: P49006), AKAP12 (UniProt ID: Q02952), HMGB2 (UniProt ID: P26583)), which adopt extended conformations with predominantly low-to-moderate p_{LDDT}, consistent with intrinsic disorder, with HMGB2 showing folded HMG boxes plus a disordered tail. Bottom row: four of the most ordered proteins (the TNT regulator CD81, ACAT1, PRDX5, GGH), which form compact, high-confidence globular folds. Coloring follows the standard AlphaFold palette (dark blue ≥ 90, cyan 70–90, yellow 50–70, orange < 50). Note that AlphaFold can assign high confidence to disorder-prone segments that fold upon binding (e.g., the stathmin and β-thymosin helices; see Figure S4). Structures are AlphaFold Database models [22].

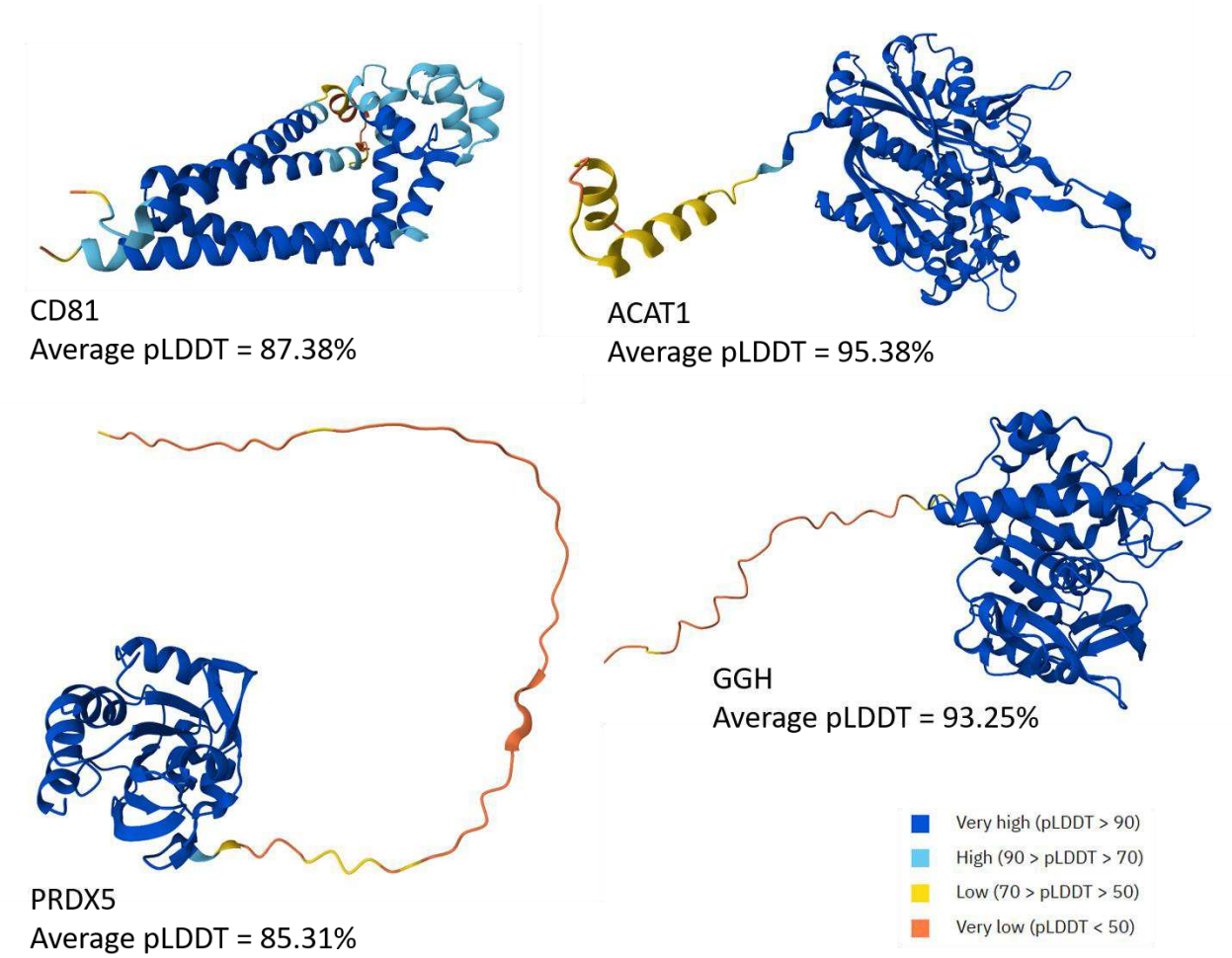


Figure 13. AlphaFold models of representative TNTome proteins at the disorder extremes, colored by per-residue confidence (p_{LDDT}). Four of the most ordered proteins (the TNT regulator CD81 (UniProt ID: P60033), ACAT1 (UniProt ID: P24752), PRDX5 (UniProt ID: Q9BGI1), GGH (UniProt ID: Q92820)), which form compact, high-confidence globular folds. The extend N-terminal tails found in ACAT1 (residues 1-33), PRDX5 (residues 1-57), and GGH (residues 1-24) correspond to transit (ACAT1 and PEDX5) and signal peptides (GGH), which act as sorting signals. Once these extensions guide the proteins to their proper destinations (the mitochondria for ACAT1 and PRDX5, and the secretory pathway for GGH), they are enzymatically cleaved to yield the mature, functional enzymes. Coloring follows the standard AlphaFold palette (dark blue ≥ 90, cyan 70–90, yellow 50–70, orange < 50). Structures are AlphaFold Database models [22].

Figure 14 provides another look at the conformational flexibility by presenting conformational ensembles generated by AFflecto [23] for HMGB2, which is the most ordered of highly disordered proteins shown in Figure 12 and for CD81, the tail-less most ordered protein from Figure 13 (see Figure 14A and 14B, respectively). Figure 14 shows that the conformational ensemble of a 209-residue-long HMGB2 occupies significantly larger volume than the conformational ensemble of the 236-residue-long CD81, reflecting larger range of structural fluctuations in HMGB2. This discrepancy fundamentally stems from differences in how these proteins are built and their physical dimensions. HMGB2 is a non-histone chromatin protein with a loose, flexible beads-on-a-string layout, granting high dynamic flexibility. Conversely, CD81 is a rigid, membrane-bound

tetraspanin that severely limits structural movement. However, Figure 14B shows that even this well-folded protein possess noticeable flexibility at its termini.

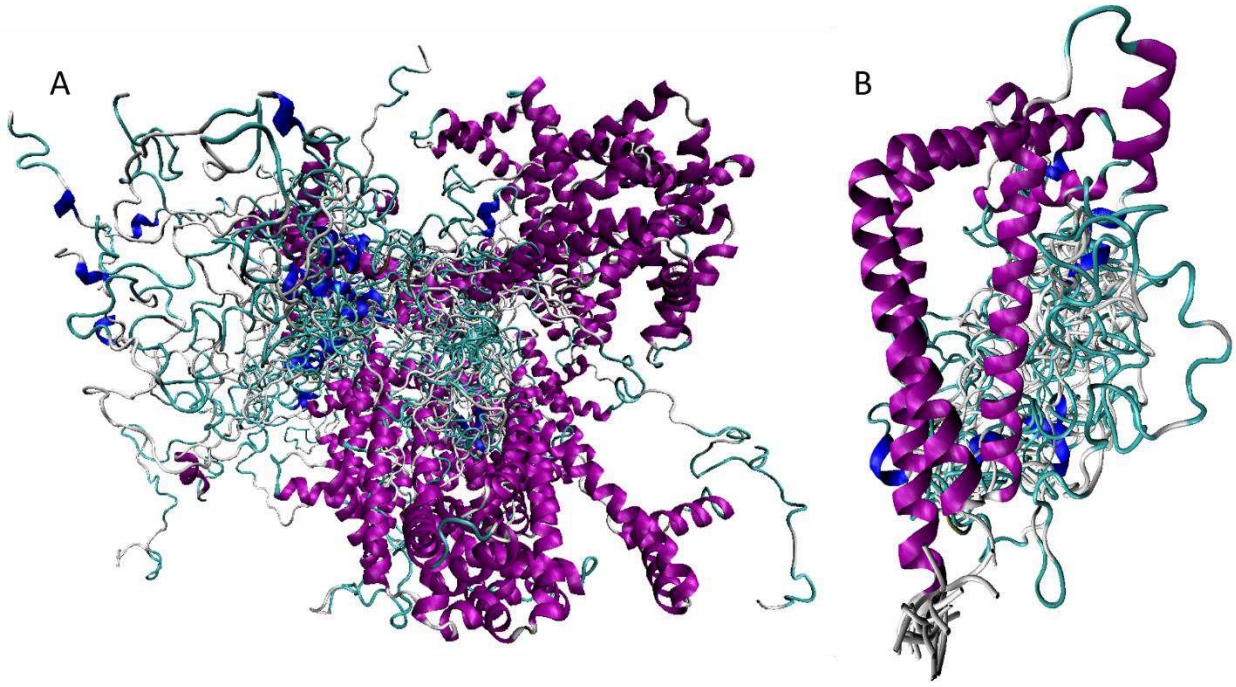


Figure 14. Conformational ensembles generated by AFflecto for HMGB2 (**A**) and CD81 (**B**). Each ensemble represents an overlay of 35 individual models. These overlays visually capture the conformational heterogeneity of analyzed proteins and effectively extend AlphaFold predictions by modeling both structured rigid domains and dynamic IDRs and thereby compensates for the limitations of AlphaFold when predicting disordered sequences. By taking an AlphaFold model as input, AFflecto identifies disordered tails, linkers, and loops, and adjusts for conditionally folded IDRs that AlphaFold might incorrectly assign as static. In this way, AFflecto addresses the biological reality that proteins function as dynamic ensembles rather than static structures.

To probe the conformational behavior of the ordered tier of human TNTome, we generated AlphaFold-based conformational ensembles for the 15 most ordered proteins with AFflecto [23]. Twelve returned ensembles of about 108 physically plausible conformers each, whereas the remaining three (GLRX, UBE2K and UBL5) contained no flexible region and yielded no ensemble (using the default AFflecto settings), marking them as the most rigid members of the set. Both the per-conformation radius of gyration (Figure 15A) and the amplitude of the most flexible region, quantified as the maximum per-residue C_α RMSF (Figure 15B), reveal a gradient of residual flexibility even among these folded proteins, ranging from essentially rigid (ESD and CD81, radius-of-gyration coefficient of variation below 1% and maximum RMSF of only 6.1 and 9.9 Å) to markedly flexible (PHB1, which carries an extended coiled-coil/low-complexity segment, radius-of-gyration coefficient of variation of 23% and maximum RMSF of 39.6 Å). Notably, several compact proteins, such as PLOD2, combine a stable overall radius of gyration with a large localized fluctuation (maximum RMSF of 34.7 Å), indicating a mobile terminus or loop on an otherwise rigid core. These observations are consistent with the view that ordered TNTome

proteins nonetheless retain mobile tails and loops, whereas the disordered tier occupies the opposite, fully flexible extreme.

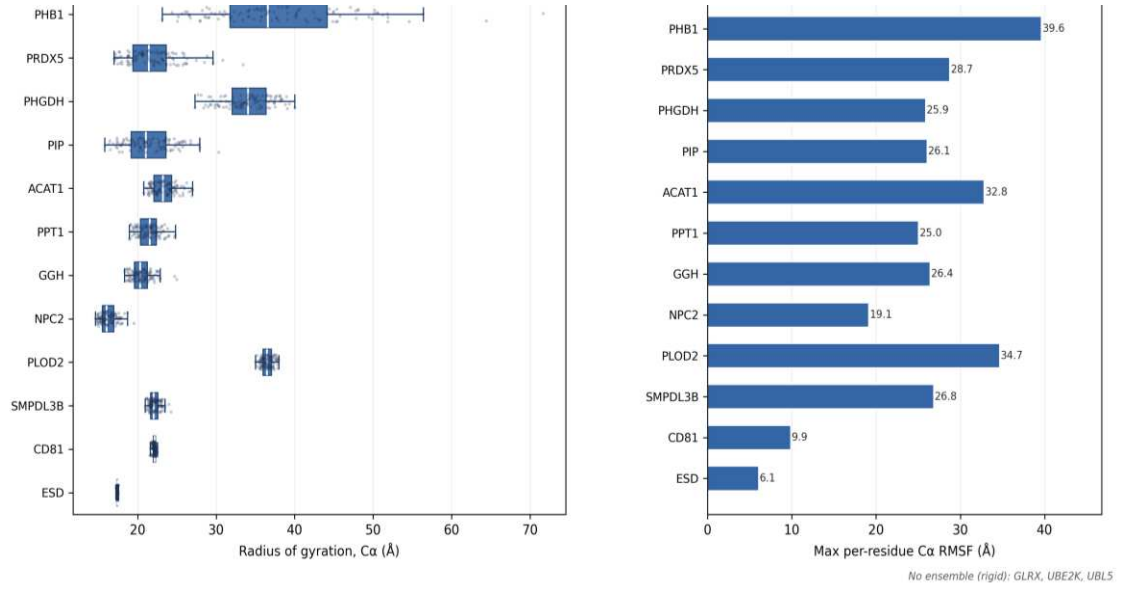


Figure 15. AFflecto conformational ensembles of the ordered TNTome proteins. (A) Distribution of the per-conformation radius of gyration (C_α) for the 12 most-ordered proteins that AFflecto could process (about 108 conformers each), ordered by ensemble spread; overlaid points are individual conformers. (B) Amplitude of the most flexible region of each protein, quantified as the maximum per-residue C_α RMSF after superposition. GLRX, UBE2K and UBL5 contained no flexible region and yielded no ensemble. Ensembles were generated from AlphaFold models with AFflecto [23].

The most striking systems-level feature is the predicted phase-separating core itself. The driver network is dominated by RNA-binding hubs, HNRNPA1, HNRNPC, HNRNPA2B1, SRSF1, SRSF3, HNRNPM, NPM1, HNRNPU and FUS, and is enriched in mRNA processing, splicing and ribonucleoprotein-complex functions, exactly the proteins for which experimental LLPS is best established: FUS [84,85], hnRNPA1 and hnRNPA2B1 [86-88], NPM1 [89,90], G3BP1 [91], YBX1 [92], SRSF1 [93], SFPQ [94] and hnRNPDL [95], with the general principle that disordered RNA-binding proteins form maturable droplets being directly demonstrated [96]. This convergence makes the prediction biologically coherent. Nevertheless, the link to TNTs remains a hypothesis: although RNA traverses TNT-like nanotubes [97], and RNA granules are known to hitchhike on organelles via tethers such as Annexin A11 [98], no study has shown any of these condensate proteins forming or tethering an RNA granule inside a TNT. The TNTome's ribonucleoprotein enrichment is therefore consistent with, but not evidence for, a phase-separated organizing layer or RNP-granule cargo in TNTs.

4.2. Healthy versus Cancerous Tunneling Nanotubes

TNTs are a general cell-biological phenomenon rather than a cancer-specific one: they were first characterized in cultured cells [1], are formed by immune cells [3], and operate in vivo in the retina [4] and in cardiac development [5], with cytoprotective mitochondrial transfer demonstrated in non-

cancer cells [99] and a broad role across brain development and neurodegeneration [6]. In tumors, however, TNT biogenesis is promoted by cancer-relevant signaling, M-Sec/TNFAIP2 and RalA [100], EGF/EGFR-dependent macrophage–tumor crosstalk [101], and mTOR-modulated formation under metabolic stress [102,103], and the best-supported functional output is mitochondrial transfer that confers chemoresistance and aggressiveness, shown from endothelium to cancer cells [104], from stroma to leukemic blasts [105], from mesenchymal stem cells to glioblastoma cells [106], and between immune and cancer cells [107]. Importantly, a direct comparison of TNTs between normal and cancerous cells now addresses whether the two differ in composition. In matched normal urothelial versus T24 bladder-cancer cells, cancer-cell TNTs were more numerous and differed in length, diameter and elasticity, and, most tellingly, were enriched in cholesterol- and sphingomyelin-rich lipid-raft nanodomains that were absent from normal-cell TNTs [108]; such nanodomains are mechanistically relevant because cholesterol-sphingomyelin membrane nanodomains stabilize intercellular nanotubes [109]. This provides a concrete membrane-compositional axis distinguishing cancer-associated from normal TNTs, complementing the tetraspanin/curvature and lipid-handling machinery highlighted above.

Two limitations bear directly on interpreting our results. First, the TNTome derives from a single cancer line (U2OS) and there is presently no mass-spectrometry-based TNT proteome from non-transformed or primary cells of comparable scope; the only prior dedicated TNT proteomics used an immortalized neuronal line at far smaller scale [110]. Second, intrinsic disorder is independently enriched in cancer-associated and signaling proteins [7], and condensate biology is itself frequently dysregulated in cancer [111]. Consequently, the disorder/LLPS enrichment we observe cannot be attributed to TNT biology as opposed to the malignant state of the source cells: the two explanations are confounded, and distinguishing them will require a non-cancer TNT proteome. We therefore present the enrichment as a property of this cancer-derived TNTome and an explicit motivation for future comparative proteomics. We re-examined this point specifically and across all candidate non-transformed cell types (primary cells, iPSC-derived cells, mesenchymal stem or stromal cells, macrophages and other immune cells, astrocytes, neurons, cardiomyocytes, and endothelial cells or pericytes) through 2026: no mass-spectrometry-based TNT proteome from non-cancer or healthy-tissue cells has been reported, confirming that the TNTome remains the only large-scale, TNT-specific isolated proteome, with the sole other dataset (Gousset et al., ~190 proteins) deriving from an immortalized mouse neuronal line [110].

4.3. Evolutionary Context: Convergence, Not Established Homology

It is tempting to relate mammalian TNTs to other intercellular conduits, but the comparison counsels caution. Bacterial nanotubes were described in Bacillus subtilis as channels for molecular exchange [112-114], with a proposed biogenesis platform based on the flagellar export apparatus [115] and regulatory links to the biofilm repressor SinR [116,117]; however, their live-cell conduit function is contested, with evidence that nanotubes are produced predominantly by dying or stressed cells [118]. Plant plasmodesmata are structurally and developmentally distinct, comprising an endoplasmic-reticulum-derived desmotubule formed during incomplete cytokinesis, with a

defined proteome and callose-based gating [119-121]. No positive molecular, sequence or structural homology links mammalian (actin-based) TNTs, bacterial (flagellar-export-associated) nanotubes and plant plasmodesmata; comparative reviews emphasize functional analogy rather than common ancestry [122-124]. Convergent evolution is therefore the parsimonious default, and any cross-kingdom evolutionary relationship should be regarded as unresolved. Recent work broadens this picture across the domains of life. Although the live-cell conduit function of Bacillus subtilis nanotubes remains contested, with evidence that they form predominantly from dying or stressed cells [118], donor-delivered cell-wall hydrolases have been shown to enable nanotube penetration into recipient bacteria [125], and independent live-cell nanotube-mediated exchange has since been documented between living marine cyanobacteria [126] and as continuous cytoplasmic cell-cell bridges in the archaeon Haloferax volcanii [127]. In plants, plasmodesmata arose independently in different lineages rather than from a single ancestral structure [128]. These observations show that intercellular conduits have evolved repeatedly across bacteria, archaea and plants without shared molecular machinery, reinforcing the convergence interpretation above.

4.4. Limitations and Open Questions

Several limitations qualify our conclusions, and each merits brief comment.

(i) All phase-separation assignments are sequence-based predictions rather than observations. Direct experimental condensate evidence now exists for only one TNTome protein, prothymosin alpha, and even that is a heterotypic coacervate with histone H1 rather than homotypic self-assembly [26]; for every other protein the FuzDrop score reports propensity, not demonstrated behavior, and family data (e.g., HMGB1 for HMGB2) must not be read as evidence for the TNTome protein itself. Experimental validation, through in vitro droplet assays and in-cell condensate imaging within TNTs, is the essential next step.

(ii) The TNTome derives from a single cancer cell line (U2OS) and no non-cancer TNT proteome of comparable scope exists, so the disorder/LLPS enrichment cannot presently be disentangled from the malignant state of the source cells; a primary-cell TNT proteome is the single most valuable next dataset.

(iii) The isolated fraction may include material co-purifying from other protrusions or subcellular compartments, so the strong nuclear/ribonucleoprotein signal of the driver network should be interpreted with caution and confirmed by orthogonal localization.

(iv) Cross-kingdom evolutionary relationships remain unresolved: no positive molecular homology links animal TNTs, bacterial nanotubes and plant plasmodesmata, and even the live-cell conduit function of *Bacillus subtilis* nanotubes is contested, so convergence is the parsimonious default rather than an established conclusion.

(v) Finally, CDV3 remains essentially uncharacterized, with disorder inferred only from prediction, and should be treated as the weakest-evidence member of the disordered set. Together these points define a clear experimental agenda: condensate assays for

candidate drivers within TNTs, a primary-cell or healthy-tissue TNT proteome, and targeted tests of whether ribonucleoprotein granules are bona fide TNT cargo.

5. Conclusions

A proteome-wide computational analysis of the U2OS TNTome shows that this intercellular-conduit proteome is structurally bimodal: 21.7% of proteins are highly disordered and 37.7% mostly ordered, and 86.6% of the highly disordered, FuzDrop-scored proteins are predicted LLPS drivers. These drivers form a dense, RNA-binding, splicing-associated interaction network whose hubs (HNRNPA1, HNRNPC, HNRNPA2B1, SRSF1, NPM1, FUS and related proteins) are among the best-established phase-separating proteins known, while the experimentally validated TNT regulators CD9 and CD81 belong to the ordered tier. We propose, as a hypothesis, a two-tier architecture in which disordered, multivalent, motif-dense scaffolds with condensate potential coexist with ordered structural and enzymatic modules. Because all LLPS calls are predictive, the two tropomyosins are retained as highly disordered monomers, and the TNTome is cancer-derived without a non-cancer counterpart, these findings are best regarded as a structured set of testable hypotheses, most pressingly, whether ribonucleoprotein condensates contribute to the organization or cargo of tunneling nanotubes, and whether the disorder/LLPS enrichment is a general property of TNTs or a feature amplified by the malignant state.

Author Contributions: Conceptualization, V.N.U.; methodology, M.A.K. and V.N.U.; formal analysis, M.A.K.; investigation, M.A.K. and V.N.U.; data curation, M.A.K. and V.N.U.; validation, A.v.d.V. and V.N.U.; writing, original draft preparation, M.A.K.; writing, review and editing; V.N.U.; editing, A.v.d.V.; supervision, V.N.U. All authors have read and agreed to the published version of the manuscript.

Acknowledgements: We are thankful to Prof. Gloria Ferreira for introducing the concept of TNTs, which inspired the study.

Funding: This research received no external funding.

Data Availability Statement: The TNTome dataset (1,177 proteins identified by mass spectrometry in TNT preparations from U2OS cells) was obtained from Supplementary file 1 of Notario Manzano et al. [2], available at https://doi.org/10.7554/eLife.99172 (https://elifesciences.org/articles/99172); the dataset file is directly accessible at https://cdn.elifesciences.org/articles/99172/elife-99172-supp1-v1.xlsx. The underlying proteomics data are deposited in the PRIDE/ProteomeXchange repository under accession PXD033089 (https://www.ebi.ac.uk/pride/archive/projects/PXD033089). All derived data (the full 1,177-protein integrated table, disorder-extremes annotations, STRING hub list, ELM motif counts and complete STRING functional-enrichment output) are provided as Supplementary Materials.

Conflicts of Interest: The authors declare no conflicts of interest.

References

1. Rustom, A.; Saffrich, R.; Markovic, I.; Walther, P.; Gerdes, H.H. Nanotubular highways for intercellular organelle transport. *Science* **2004**, *303*, 1007-1010, doi:10.1126/science.1093133.

2. Notario Manzano, R.; Chaze, T.; Rubinstein, E.; Penard, E.; Matondo, M.; Zurzolo, C.; Brou, C. Proteomic landscape of tunneling nanotubes reveals CD9 and CD81 tetraspanins as key regulators. *Elife* **2024**, *13*, doi:10.7554/eLife.99172.

3. Onfelt, B.; Nedvetzki, S.; Yanagi, K.; Davis, D.M. Cutting edge: Membrane nanotubes connect immune cells. *J Immunol* **2004**, *173*, 1511-1513, doi:10.4049/jimmunol.173.3.1511.

4. Ortin-Martinez, A.; Yan, N.E.; Tsai, E.L.S.; Comanita, L.; Gurdita, A.; Tachibana, N.; Liu, Z.C.; Lu, S.; Dolati, P.; Pokrajac, N.T.; et al. Photoreceptor nanotubes mediate the in vivo exchange of intracellular material. *EMBO J* **2021**, *40*, e107264, doi:10.15252/embj.2020107264.

5. Chen, T.; Ellman, D.G.; Fang, S.; Bak, S.T.; Norgard, M.O.; Svenningsen, P.; Andersen, D.C. Transfer of cardiomyocyte-derived extracellular vesicles to neighboring cardiac cells requires tunneling nanotubes during heart development. *Theranostics* **2024**, *14*, 3843-3858, doi:10.7150/thno.91604.

6. Palese, F.; Rakotobe, M.; Zurzolo, C. Transforming the concept of connectivity: unveiling tunneling nanotube biology and their roles in brain development and neurodegeneration. *Physiol Rev* **2025**, *105*, 1823-1865, doi:10.1152/physrev.00023.2024.

7. Iakoucheva, L.M.; Brown, C.J.; Lawson, J.D.; Obradovic, Z.; Dunker, A.K. Intrinsic disorder in cell-signaling and cancer-associated proteins. *J Mol Biol* **2002**, *323*, 573-584, doi:10.1016/s0022-2836(02)00969-5.

8. Li, P.; Banjade, S.; Cheng, H.C.; Kim, S.; Chen, B.; Guo, L.; Llaguno, M.; Hollingsworth, J.V.; King, D.S.; Banani, S.F.; et al. Phase transitions in the assembly of multivalent signalling proteins. *Nature* **2012**, *483*, 336-340, doi:10.1038/nature10879.

9. Brangwynne, C.P.; Eckmann, C.R.; Courson, D.S.; Rybarska, A.; Hoege, C.; Gharakhani, J.; Julicher, F.; Hyman, A.A. Germline P granules are liquid droplets that localize by controlled dissolution/condensation. *Science* **2009**, *324*, 1729-1732, doi:10.1126/science.1172046.

10. Wang, J.; Choi, J.M.; Holehouse, A.S.; Lee, H.O.; Zhang, X.; Jahnel, M.; Maharana, S.; Lemaitre, R.; Pozniakovsky, A.; Drechsel, D.; et al. A Molecular Grammar Governing the Driving Forces for Phase Separation of Prion-like RNA Binding Proteins. *Cell* **2018**, *174*, 688-699 e616, doi:10.1016/j.cell.2018.06.006.

11. Banani, S.F.; Lee, H.O.; Hyman, A.A.; Rosen, M.K. Biomolecular condensates: organizers of cellular biochemistry. *Nat Rev Mol Cell Biol* **2017**, *18*, 285-298, doi:10.1038/nrm.2017.7.

12. Dayhoff, G.W., 2nd; Uversky, V.N. Rapid prediction and analysis of protein intrinsic disorder. *Protein Sci* **2022**, *31*, e4496, doi:10.1002/pro.4496.

13. Uversky, V.N.; Gillespie, J.R.; Fink, A.L. Why are "natively unfolded" proteins unstructured under physiologic conditions? *Proteins* **2000**, *41*, 415-427, doi:10.1002/1097-0134(20001115)41:3<415::aid-prot130>3.0.co;2-7.

14. Xue, B.; Oldfield, C.J.; Dunker, A.K.; Uversky, V.N. CDF it all: consensus prediction of intrinsically disordered proteins based on various cumulative distribution functions. *FEBS Lett* **2009**, *583*, 1469-1474, doi:10.1016/j.febslet.2009.03.070.

15. Oates, M.E.; Romero, P.; Ishida, T.; Ghalwash, M.; Mizianty, M.J.; Xue, B.; Dosztanyi, Z.; Uversky, V.N.; Obradovic, Z.; Kurgan, L.; et al. D(2)P(2): database of disordered protein predictions. *Nucleic Acids Res* **2013**, *41*, D508-516, doi:10.1093/nar/gks1226.

16. Hardenberg, M.; Horvath, A.; Ambrus, V.; Fuxreiter, M.; Vendruscolo, M. Widespread occurrence of the droplet state of proteins in the human proteome. *Proc Natl Acad Sci U S A* **2020**, *117*, 33254-33262, doi:10.1073/pnas.2007670117.

17. Hatos, A.; Tosatto, S.C.E.; Vendruscolo, M.; Fuxreiter, M. FuzDrop on AlphaFold: visualizing the sequence-dependent propensity of liquid-liquid phase separation and aggregation of proteins. *Nucleic Acids Res* **2022**, *50*, W337-W344, doi:10.1093/nar/gkac386.

18. Gouw, M.; Michael, S.; Samano-Sanchez, H.; Kumar, M.; Zeke, A.; Lang, B.; Bely, B.; Chemes, L.B.; Davey, N.E.; Deng, Z.; et al. The eukaryotic linear motif resource - 2018 update. *Nucleic Acids Res* **2018**, *46*, D428-D434, doi:10.1093/nar/gkx1077.

19. Szklarczyk, D.; Kirsch, R.; Koutrouli, M.; Nastou, K.; Mehryary, F.; Hachilif, R.; Gable, A.L.; Fang, T.; Doncheva, N.T.; Pyysalo, S.; et al. The STRING database in 2023: protein-protein association networks and functional enrichment analyses for any sequenced genome of interest. *Nucleic Acids Res* **2023**, *51*, D638-D646, doi:10.1093/nar/gkac1000.

20. Kanehisa, M.; Goto, S. KEGG: Kyoto Encyclopedia of Genes and Genomes. *Nucleic Acids Res* **2000**, *28*, 27-30, doi:10.1093/nar/28.1.27.

21. Kanehisa, M.; Furumichi, M.; Sato, Y.; Matsuura, Y.; Ishiguro-Watanabe, M. KEGG: biological systems database as a model of the real world. *Nucleic Acids Res* **2025**, *53*, D672-D677, doi:10.1093/nar/gkae909.

22. Jumper, J.; Evans, R.; Pritzel, A.; Green, T.; Figurnov, M.; Ronneberger, O.; Tunyasuvunakool, K.; Bates, R.; Zidek, A.; Potapenko, A.; et al. Highly accurate protein structure prediction with AlphaFold. *Nature* **2021**, *596*, 583-589, doi:10.1038/s41586-021-03819-2.

23. Pajkos, M.; Clerc, I.; Zanon, C.; Bernado, P.; Cortes, J. AFflecto: A web server to generate conformational ensembles of flexible proteins from AlphaFold models. *J Mol Biol* **2025**, *437*, 169003, doi:10.1016/j.jmb.2025.169003.

24. Uhlen, M.; Fagerberg, L.; Hallstrom, B.M.; Lindskog, C.; Oksvold, P.; Mardinoglu, A.; Sivertsson, A.; Kampf, C.; Sjostedt, E.; Asplund, A.; et al. Proteomics. Tissue-based map of the human proteome. *Science* **2015**, *347*, 1260419, doi:10.1126/science.1260419.

25. Antonietti, M.; Taylor Gonzalez, D.J.; Djulbegovic, M.B.; Gameiro, G.R.; Uversky, V.N.; Sridhar, J.; Karp, C.L. Intrinsic disorder in the human vitreous proteome. *Int J Biol Macromol* **2024**, *267*, 131274, doi:10.1016/j.ijbiomac.2024.131274.

26. Galvanetto, N.; Ivanovic, M.T.; Chowdhury, A.; Sottini, A.; Nuesch, M.F.; Nettels, D.; Best, R.B.; Schuler, B. Extreme dynamics in a biomolecular condensate. *Nature* **2023**, *619*, 876-883, doi:10.1038/s41586-023-06329-5.

27. Uversky, V.N.; Gillespie, J.R.; Millett, I.S.; Khodyakova, A.V.; Vasiliev, A.M.; Chernovskaya, T.V.; Vasilenko, R.N.; Kozlovskaya, G.D.; Dolgikh, D.A.; Fink, A.L.; et al. Natively unfolded human prothymosin alpha adopts partially folded collapsed conformation at acidic pH. *Biochemistry* **1999**, *38*, 15009-15016, doi:10.1021/bi990752+.

28. Borgia, A.; Borgia, M.B.; Bugge, K.; Kissling, V.M.; Heidarsson, P.O.; Fernandes, C.B.; Sottini, A.; Soranno, A.; Buholzer, K.J.; Nettels, D.; et al. Extreme disorder in an ultrahigh-affinity protein complex. *Nature* **2018**, *555*, 61-66, doi:10.1038/nature25762.

29. Heidarsson, P.O.; Mercadante, D.; Sottini, A.; Nettels, D.; Borgia, M.B.; Borgia, A.; Kilic, S.; Fierz, B.; Best, R.B.; Schuler, B. Release of linker histone from the nucleosome driven by polyelectrolyte competition with a disordered protein. *Nat Chem* **2022**, *14*, 224-231, doi:10.1038/s41557-021-00839-3.

30. Martic, G.; Karetsou, Z.; Kefala, K.; Politou, A.S.; Clapier, C.R.; Straub, T.; Papamarcaki, T. Parathymosin affects the binding of linker histone H1 to nucleosomes and remodels chromatin structure. *J Biol Chem* **2005**, *280*, 16143-16150, doi:10.1074/jbc.M410175200.

31. Irobi, E.; Aguda, A.H.; Larsson, M.; Guerin, C.; Yin, H.L.; Burtnick, L.D.; Blanchoin, L.; Robinson, R.C. Structural basis of actin sequestration by thymosin-beta4: implications for WH2 proteins. *EMBO J* **2004**, *23*, 3599-3608, doi:10.1038/sj.emboj.7600372.

32. Bjorkblom, B.; Padzik, A.; Mohammad, H.; Westerlund, N.; Komulainen, E.; Hollos, P.; Parviainen, L.; Papageorgiou, A.C.; Iljin, K.; Kallioniemi, O.; et al. c-Jun N-terminal kinase phosphorylation of MARCKSL1 determines actin stability and migration in neurons and in cancer cells. *Mol Cell Biol* **2012**, *32*, 3513-3526, doi:10.1128/MCB.00713-12.

33. Graham, K.; Chandrasekaran, A.; Wang, L.; Ladak, A.; Lafer, E.M.; Rangamani, P.; Stachowiak, J.C. Liquid-like VASP condensates drive actin polymerization and dynamic bundling. *Nat Phys* **2023**, *19*, 574-585, doi:10.1038/s41567-022-01924-1.

34. Karpova, N.; Bobinnec, Y.; Fouix, S.; Huitorel, P.; Debec, A. Jupiter, a new Drosophila protein associated with microtubules. *Cell Motil Cytoskeleton* **2006**, *63*, 301-312, doi:10.1002/cm.20124.

35. Li, H.; Fan, S.; Gong, Z.; Chan, J.Y.K.; Tong, M.C.F.; Chen, G.G. Role of hematological and neurological expressed 1 (HN1) in human cancers. *Crit Rev Oncol Hematol* **2024**, *201*, 104446, doi:10.1016/j.critrevonc.2024.104446.

36. Gunaratne, G.S.; Brailoiu, E.; He, S.; Unterwald, E.M.; Patel, S.; Slama, J.T.; Walseth, T.F.; Marchant, J.S. Essential requirement for JPT2 in NAADP-evoked Ca(2+) signaling. *Sci Signal* **2021**, *14*, doi:10.1126/scisignal.abd5605.

37. Gelman, I.H. Emerging Roles for SSeCKS/Gravin/AKAP12 in the Control of Cell Proliferation, Cancer Malignancy, and Barriergenesis. *Genes Cancer* **2010**, *1*, 1147-1156, doi:10.1177/1947601910392984.

38. Watson, M.; Almeida, T.B.; Ray, A.; Hanack, C.; Elston, R.; Btesh, J.; McNaughton, P.A.; Stott, K. Hidden Multivalency in Phosphatase Recruitment by a Disordered AKAP Scaffold. *J Mol Biol* **2022**, *434*, 167682, doi:10.1016/j.jmb.2022.167682.

39. Wells, J.N.; Buschauer, R.; Mackens-Kiani, T.; Best, K.; Kratzat, H.; Berninghausen, O.; Becker, T.; Gilbert, W.; Cheng, J.; Beckmann, R. Structure and function of yeast Lso2 and human CCDC124 bound to hibernating ribosomes. *PLoS Biol* **2020**, *18*, e3000780, doi:10.1371/journal.pbio.3000780.

40. Telkoparan, P.; Erkek, S.; Yaman, E.; Alotaibi, H.; Bayik, D.; Tazebay, U.H. Coiled-coil domain containing protein 124 is a novel centrosome and midbody protein that interacts with the Ras-guanine nucleotide exchange factor 1B and is involved in cytokinesis. *PLoS One* **2013**, *8*, e69289, doi:10.1371/journal.pone.0069289.

41. Starkova, T.; Polyanichko, A.; Tomilin, A.N.; Chikhirzhina, E. Structure and Functions of HMGB2 Protein. *Int J Mol Sci* **2023**, *24*, doi:10.3390/ijms24098334.

42. Zirkel, A.; Nikolic, M.; Sofiadis, K.; Mallm, J.P.; Brackley, C.A.; Gothe, H.; Drechsel, O.; Becker, C.; Altmuller, J.; Josipovic, N.; et al. HMGB2 Loss upon Senescence Entry Disrupts Genomic Organization and Induces CTCF Clustering across Cell Types. *Mol Cell* **2018**, *70*, 730-744 e736, doi:10.1016/j.molcel.2018.03.030.

43. Gigant, B.; Curmi, P.A.; Martin-Barbey, C.; Charbaut, E.; Lachkar, S.; Lebeau, L.; Siavoshian, S.; Sobel, A.; Knossow, M. The 4 A X-ray structure of a tubulin:stathmin-like domain complex. *Cell* **2000**, *102*, 809-816, doi:10.1016/s0092-8674(00)00069-6.

44. Steinmetz, M.O. Structure and thermodynamics of the tubulin-stathmin interaction. *J Struct Biol* **2007**, *158*, 137-147, doi:10.1016/j.jsb.2006.07.018.

45. Chui, A.J.; Lopez, C.J.; Brooks, E.K.; Chua, K.C.; Doupey, T.G.; Foltz, G.N.; Kamel, J.G.; Larrosa, E.; Sadiki, A.; Bridges, M.D. Multiple structural states exist throughout the helical nucleation sequence of the intrinsically disordered protein stathmin, as reported by electron paramagnetic resonance spectroscopy. *Biochemistry* **2015**, *54*, 1717-1728, doi:10.1021/bi500894q.

46. Miller, S.A.; Brown, A.J.; Farach-Carson, M.C.; Kirn-Safran, C.B. HIP/RPL29 down-regulation accompanies terminal chondrocyte differentiation. *Differentiation* **2003**, *71*, 322-336, doi:10.1046/j.1432-0436.2003.7106002.x.

47. Hacibeyoglu, K.; Tuzlakoglu Ozturk, M.; Arslan, O.; Tazebay, U.H. Live Cell Protein Imaging of Tandem Complemented-GFP11-Tagged Coiled-Coil Domain-Containing Protein-124 Identifies this Factor in G3BP1-Induced Stress-Granules. *Protein J* **2024**, *43*, 834-841, doi:10.1007/s10930-024-10216-x.

48. Tuzlakoglu Ozturk, M.; Gullulu, O. Dimerization underlies the aggregation propensity of intrinsically disordered coiled-coil domain-containing 124. *Proteins* **2022**, *90*, 218-228, doi:10.1002/prot.26210.

49. Kondrychyn, I.; Kelly, D.J.; Carretero, N.T.; Nomori, A.; Kato, K.; Chong, J.; Nakajima, H.; Okuda, S.; Mochizuki, N.; Phng, L.K. Marcksl1 modulates endothelial cell mechanoresponse to haemodynamic forces to control blood vessel shape and size. *Nat Commun* **2020**, *11*, 5476, doi:10.1038/s41467-020-19308-5.

50. Kitadokoro, K.; Bordo, D.; Galli, G.; Petracca, R.; Falugi, F.; Abrignani, S.; Grandi, G.; Bolognesi, M. CD81 extracellular domain 3D structure: insight into the tetraspanin superfamily structural motifs. *EMBO J* **2001**, *20*, 12-18, doi:10.1093/emboj/20.1.12.

51. Zimmerman, B.; Kelly, B.; McMillan, B.J.; Seegar, T.C.M.; Dror, R.O.; Kruse, A.C.; Blacklow, S.C. Crystal Structure of a Full-Length Human Tetraspanin Reveals a Cholesterol-Binding Pocket. *Cell* **2016**, *167*, 1041-1051 e1011, doi:10.1016/j.cell.2016.09.056.

52. Susa, K.J.; Rawson, S.; Kruse, A.C.; Blacklow, S.C. Cryo-EM structure of the B cell co-receptor CD19 bound to the tetraspanin CD81. *Science* **2021**, *371*, 300-305, doi:10.1126/science.abd9836.

53. Umeda, R.; Satouh, Y.; Takemoto, M.; Nakada-Nakura, Y.; Liu, K.; Yokoyama, T.; Shirouzu, M.; Iwata, S.; Nomura, N.; Sato, K.; et al. Structural insights into tetraspanin CD9 function. *Nat Commun* **2020**, *11*, 1606, doi:10.1038/s41467-020-15459-7.

54. Oosterheert, W.; Xenaki, K.T.; Neviani, V.; Pos, W.; Doulkeridou, S.; Manshande, J.; Pearce, N.M.; Kroon-Batenburg, L.M.; Lutz, M.; van Bergen En Henegouwen, P.M.; et al. Implications for tetraspanin-enriched microdomain assembly based on structures of CD9 with EWI-F. *Life Sci Alliance* **2020**, *3*, doi:10.26508/lsa.202000883.

55. Haapalainen, A.M.; Merilainen, G.; Pirila, P.L.; Kondo, N.; Fukao, T.; Wierenga, R.K. Crystallographic and kinetic studies of human mitochondrial acetoacetyl-CoA thiolase: the importance of potassium and chloride ions for its structure and function. *Biochemistry* **2007**, *46*, 4305-4321, doi:10.1021/bi6026192.

56. Fan, J.; Lin, R.; Xia, S.; Chen, D.; Elf, S.E.; Liu, S.; Pan, Y.; Xu, H.; Qian, Z.; Wang, M.; et al. Tetrameric Acetyl-CoA Acetyltransferase 1 Is Important for Tumor Growth. *Mol Cell* **2016**, *64*, 859-874, doi:10.1016/j.molcel.2016.10.014.

57. Possemato, R.; Marks, K.M.; Shaul, Y.D.; Pacold, M.E.; Kim, D.; Birsoy, K.; Sethumadhavan, S.; Woo, H.K.; Jang, H.G.; Jha, A.K.; et al. Functional genomics reveal that the serine synthesis pathway is essential in breast cancer. *Nature* **2011**, *476*, 346-350, doi:10.1038/nature10350.

58. Lange, F.; Ratz, M.; Dohrke, J.N.; Le Vasseur, M.; Wenzel, D.; Ilgen, P.; Riedel, D.; Jakobs, S. In situ architecture of the human prohibitin complex. *Nat Cell Biol* **2025**, *27*, 633-640, doi:10.1038/s41556-025-01620-1.

59. Bellizzi, J.J., 3rd; Widom, J.; Kemp, C.; Lu, J.Y.; Das, A.K.; Hofmann, S.L.; Clardy, J. The crystal structure of palmitoyl protein thioesterase 1 and the molecular basis of infantile neuronal ceroid lipofuscinosis. *Proc Natl Acad Sci U S A* **2000**, *97*, 4573-4578, doi:10.1073/pnas.080508097.

60. Calero, G.; Gupta, P.; Nonato, M.C.; Tandel, S.; Biehl, E.R.; Hofmann, S.L.; Clardy, J. The crystal structure of palmitoyl protein thioesterase-2 (PPT2) reveals the basis for divergent substrate specificities of the two lysosomal thioesterases, PPT1 and PPT2. *J Biol Chem* **2003**, *278*, 37957-37964, doi:10.1074/jbc.M301225200.

61. Friedland, N.; Liou, H.L.; Lobel, P.; Stock, A.M. Structure of a cholesterol-binding protein deficient in Niemann-Pick type C2 disease. *Proc Natl Acad Sci U S A* **2003**, *100*, 2512-2517, doi:10.1073/pnas.0437840100.

62. Li, X.; Saha, P.; Li, J.; Blobel, G.; Pfeffer, S.R. Clues to the mechanism of cholesterol transfer from the structure of NPC1 middle lumenal domain bound to NPC2. *Proc Natl Acad Sci U S A* **2016**, *113*, 10079-10084, doi:10.1073/pnas.1611956113.

63. Juhl, A.D.; Lund, F.W.; Jensen, M.L.V.; Szomek, M.; Heegaard, C.W.; Guttmann, P.; Werner, S.; McNally, J.; Schneider, G.; Kapishnikov, S.; et al. Niemann Pick C2 protein enables cholesterol transfer from endo-lysosomes to the plasma membrane for efflux by shedding of extracellular vesicles. *Chem Phys Lipids* **2021**, *235*, 105047, doi:10.1016/j.chemphyslip.2020.105047.

64. Gorelik, A.; Heinz, L.X.; Illes, K.; Superti-Furga, G.; Nagar, B. Crystal Structure of the Acid Sphingomyelinase-like Phosphodiesterase SMPDL3B Provides Insights into Determinants of Substrate Specificity. *J Biol Chem* **2016**, *291*, 24054-24064, doi:10.1074/jbc.M116.755801.

65. Heinz, L.X.; Baumann, C.L.; Koberlin, M.S.; Snijder, B.; Gawish, R.; Shui, G.; Sharif, O.; Aspalter, I.M.; Muller, A.C.; Kandasamy, R.K.; et al. The Lipid-Modifying Enzyme SMPDL3B Negatively Regulates Innate Immunity. *Cell Rep* **2015**, *11*, 1919-1928, doi:10.1016/j.celrep.2015.05.006.

66. Li, H.; Ryan, T.J.; Chave, K.J.; Van Roey, P. Three-dimensional structure of human gamma -glutamyl hydrolase. A class I glatamine amidotransferase adapted for a complex substate. *J Biol Chem* **2002**, *277*, 24522-24529, doi:10.1074/jbc.M202020200.

67. Wu, D.; Li, Y.; Song, G.; Zhang, D.; Shaw, N.; Liu, Z.J. Crystal structure of human esterase D: a potential genetic marker of retinoblastoma. *FASEB J* **2009**, *23*, 1441-1446, doi:10.1096/fj.08-125286.

68. Lee, W.H.; Wheatley, W.; Benedict, W.F.; Huang, C.M.; Lee, E.Y. Purification, biochemical characterization, and biological function of human esterase D. *Proc Natl Acad Sci U S A* **1986**, *83*, 6790-6794, doi:10.1073/pnas.83.18.6790.

69. Declercq, J.P.; Evrard, C.; Clippe, A.; Stricht, D.V.; Bernard, A.; Knoops, B. Crystal structure of human peroxiredoxin 5, a novel type of mammalian peroxiredoxin at 1.5 A resolution. *J Mol Biol* **2001**, *311*, 751-759, doi:10.1006/jmbi.2001.4853.

70. Smeets, A.; Marchand, C.; Linard, D.; Knoops, B.; Declercq, J.P. The crystal structures of oxidized forms of human peroxiredoxin 5 with an intramolecular disulfide bond confirm the proposed enzymatic mechanism for atypical 2-Cys peroxiredoxins. *Arch Biochem Biophys* **2008**, *477*, 98-104, doi:10.1016/j.abb.2008.04.036.

71. Poncin, M.A.; Van Meerbeeck, P.; Simpson, J.D.; Clippe, A.; Tyckaert, F.; Bouillenne, F.; Degand, H.; Matagne, A.; Morsomme, P.; Knoops, B.; et al. Role of the Redox State of Human

Peroxiredoxin-5 on Its TLR4-Activating DAMP Function. *Antioxidants (Basel)* **2021**, *10*, doi:10.3390/antiox10121902.

72. Sun, C.; Berardi, M.J.; Bushweller, J.H. The NMR solution structure of human glutaredoxin in the fully reduced form. *J Mol Biol* **1998**, *280*, 687-701, doi:10.1006/jmbi.1998.1913.

73. Sakai, J.; Li, J.; Subramanian, K.K.; Mondal, S.; Bajrami, B.; Hattori, H.; Jia, Y.; Dickinson, B.C.; Zhong, J.; Ye, K.; et al. Reactive oxygen species-induced actin glutathionylation controls actin dynamics in neutrophils. *Immunity* **2012**, *37*, 1037-1049, doi:10.1016/j.immuni.2012.08.017.

74. Mishra, S.K.; Ammon, T.; Popowicz, G.M.; Krajewski, M.; Nagel, R.J.; Ares, M., Jr.; Holak, T.A.; Jentsch, S. Role of the ubiquitin-like protein Hub1 in splice-site usage and alternative splicing. *Nature* **2011**, *474*, 173-178, doi:10.1038/nature10143.

75. Ammon, T.; Mishra, S.K.; Kowalska, K.; Popowicz, G.M.; Holak, T.A.; Jentsch, S. The conserved ubiquitin-like protein Hub1 plays a critical role in splicing in human cells. *J Mol Cell Biol* **2014**, *6*, 312-323, doi:10.1093/jmcb/mju026.

76. Wilson, R.C.; Hughes, R.C.; Flatt, J.W.; Meehan, E.J.; Ng, J.D.; Twigg, P.D. Structure of full-length ubiquitin-conjugating enzyme E2-25K (huntingtin-interacting protein 2). *Acta Crystallogr Sect F Struct Biol Cryst Commun* **2009**, *65*, 440-444, doi:10.1107/S1744309109011117.

77. Wilson, R.C.; Edmondson, S.P.; Flatt, J.W.; Helms, K.; Twigg, P.D. The E2-25K ubiquitin-associated (UBA) domain aids in polyubiquitin chain synthesis and linkage specificity. *Biochem Biophys Res Commun* **2011**, *405*, 662-666, doi:10.1016/j.bbrc.2011.01.089.

78. Hassan, M.I.; Bilgrami, S.; Kumar, V.; Singh, N.; Yadav, S.; Kaur, P.; Singh, T.P. Crystal structure of the novel complex formed between zinc alpha2-glycoprotein (ZAG) and prolactin-inducible protein (PIP) from human seminal plasma. *J Mol Biol* **2008**, *384*, 663-672, doi:10.1016/j.jmb.2008.09.072.

79. Urbaniak, A.; Jablonska, K.; Podhorska-Okolow, M.; Ugorski, M.; Dziegiel, P. Prolactin-induced protein (PIP)-characterization and role in breast cancer progression. *Am J Cancer Res* **2018**, *8*, 2150-2164.

80. Scietti, L.; Chiapparino, A.; De Giorgi, F.; Fumagalli, M.; Khoriauli, L.; Nergadze, S.; Basu, S.; Olieric, V.; Cucca, L.; Banushi, B.; et al. Molecular architecture of the multifunctional collagen lysyl hydroxylase and glycosyltransferase LH3. *Nat Commun* **2018**, *9*, 3163, doi:10.1038/s41467-018-05631-5.

81. Peng, J.; Li, W.; Yao, D.; Xia, Y.; Wang, Q.; Cai, Y.; Li, S.; Cao, M.; Shen, Y.; Ma, P.; et al. The structural basis for the human procollagen lysine hydroxylation and dual-glycosylation. *Nat Commun* **2025**, *16*, 2436, doi:10.1038/s41467-025-57768-9.

82. Chen, Y.; Guo, H.; Terajima, M.; Banerjee, P.; Liu, X.; Yu, J.; Momin, A.A.; Katayama, H.; Hanash, S.M.; Burns, A.R.; et al. Lysyl Hydroxylase 2 Is Secreted by Tumor Cells and Can Modify Collagen in the Extracellular Space. *J Biol Chem* **2016**, *291*, 25799-25808, doi:10.1074/jbc.M116.759803.

83. Dharan, R.; Goren, S.; Cheppali, S.K.; Shendrik, P.; Brand, G.; Vaknin, A.; Yu, L.; Kozlov, M.M.; Sorkin, R. Transmembrane proteins tetraspanin 4 and CD9 sense membrane curvature. *Proc Natl Acad Sci U S A* **2022**, *119*, e2208993119, doi:10.1073/pnas.2208993119.

84. Patel, A.; Lee, H.O.; Jawerth, L.; Maharana, S.; Jahnel, M.; Hein, M.Y.; Stoynov, S.; Mahamid, J.; Saha, S.; Franzmann, T.M.; et al. A Liquid-to-Solid Phase Transition of the ALS Protein FUS Accelerated by Disease Mutation. *Cell* **2015**, *162*, 1066-1077, doi:10.1016/j.cell.2015.07.047.

85. Kato, M.; Han, T.W.; Xie, S.; Shi, K.; Du, X.; Wu, L.C.; Mirzaei, H.; Goldsmith, E.J.; Longgood, J.; Pei, J.; et al. Cell-free formation of RNA granules: low complexity sequence domains form dynamic fibers within hydrogels. *Cell* **2012**, *149*, 753-767, doi:10.1016/j.cell.2012.04.017.

86. Molliex, A.; Temirov, J.; Lee, J.; Coughlin, M.; Kanagaraj, A.P.; Kim, H.J.; Mittag, T.; Taylor, J.P. Phase separation by low complexity domains promotes stress granule assembly and drives pathological fibrillization. *Cell* **2015**, *163*, 123-133, doi:10.1016/j.cell.2015.09.015.

87. Kim, H.J.; Kim, N.C.; Wang, Y.D.; Scarborough, E.A.; Moore, J.; Diaz, Z.; MacLea, K.S.; Freibaum, B.; Li, S.; Molliex, A.; et al. Mutations in prion-like domains in hnRNPA2B1 and hnRNPA1 cause multisystem proteinopathy and ALS. *Nature* **2013**, *495*, 467-473, doi:10.1038/nature11922.

88. Ryan, V.H.; Dignon, G.L.; Zerze, G.H.; Chabata, C.V.; Silva, R.; Conicella, A.E.; Amaya, J.; Burke, K.A.; Mittal, J.; Fawzi, N.L. Mechanistic View of hnRNPA2 Low-Complexity Domain Structure, Interactions, and Phase Separation Altered by Mutation and Arginine Methylation. *Mol Cell* **2018**, *69*, 465-479 e467, doi:10.1016/j.molcel.2017.12.022.

89. Mitrea, D.M.; Cika, J.A.; Guy, C.S.; Ban, D.; Banerjee, P.R.; Stanley, C.B.; Nourse, A.; Deniz, A.A.; Kriwacki, R.W. Nucleophosmin integrates within the nucleolus via multi-modal interactions with proteins displaying R-rich linear motifs and rRNA. *Elife* **2016**, *5*, doi:10.7554/eLife.13571.

90. Feric, M.; Vaidya, N.; Harmon, T.S.; Mitrea, D.M.; Zhu, L.; Richardson, T.M.; Kriwacki, R.W.; Pappu, R.V.; Brangwynne, C.P. Coexisting Liquid Phases Underlie Nucleolar Subcompartments. *Cell* **2016**, *165*, 1686-1697, doi:10.1016/j.cell.2016.04.047.

91. Yang, P.; Mathieu, C.; Kolaitis, R.M.; Zhang, P.; Messing, J.; Yurtsever, U.; Yang, Z.; Wu, J.; Li, Y.; Pan, Q.; et al. G3BP1 Is a Tunable Switch that Triggers Phase Separation to Assemble Stress Granules. *Cell* **2020**, *181*, 325-345 e328, doi:10.1016/j.cell.2020.03.046.

92. Liu, X.M.; Ma, L.; Schekman, R. Selective sorting of microRNAs into exosomes by phase-separated YBX1 condensates. *Elife* **2021**, *10*, doi:10.7554/eLife.71982.

93. Fargason, T.; De Silva, N.I.U.; Powell, E.; Zhang, Z.; Paul, T.; Shariq, J.; Zaharias, S.; Zhang, J. Peptides that Mimic RS repeats modulate phase separation of SRSF1, revealing a reliance on combined stacking and electrostatic interactions. *Elife* **2023**, *12*, doi:10.7554/eLife.84412.

94. Lee, M.; Sadowska, A.; Bekere, I.; Ho, D.; Gully, B.S.; Lu, Y.; Iyer, K.S.; Trewhella, J.; Fox, A.H.; Bond, C.S. The structure of human SFPQ reveals a coiled-coil mediated polymer essential for functional aggregation in gene regulation. *Nucleic Acids Res* **2015**, *43*, 3826-3840, doi:10.1093/nar/gkv156.

95. Batlle, C.; Yang, P.; Coughlin, M.; Messing, J.; Pesarrodona, M.; Szulc, E.; Salvatella, X.; Kim, H.J.; Taylor, J.P.; Ventura, S. hnRNPDL Phase Separation Is Regulated by Alternative Splicing and Disease-Causing Mutations Accelerate Its Aggregation. *Cell Rep* **2020**, *30*, 1117-1128 e1115, doi:10.1016/j.celrep.2019.12.080.

96. Lin, Y.; Protter, D.S.; Rosen, M.K.; Parker, R. Formation and Maturation of Phase-Separated Liquid Droplets by RNA-Binding Proteins. *Mol Cell* **2015**, *60*, 208-219, doi:10.1016/j.molcel.2015.08.018.

97. Haimovich, G.; Ecker, C.M.; Dunagin, M.C.; Eggan, E.; Raj, A.; Gerst, J.E.; Singer, R.H. Intercellular mRNA trafficking via membrane nanotube-like extensions in mammalian cells. *Proc Natl Acad Sci U S A* **2017**, *114*, E9873-E9882, doi:10.1073/pnas.1706365114.

98. Liao, Y.C.; Fernandopulle, M.S.; Wang, G.; Choi, H.; Hao, L.; Drerup, C.M.; Patel, R.; Qamar, S.; Nixon-Abell, J.; Shen, Y.; et al. RNA Granules Hitchhike on Lysosomes for Long-Distance

Transport, Using Annexin A11 as a Molecular Tether. *Cell* **2019**, *179*, 147-164 e120, doi:10.1016/j.cell.2019.08.050.

99. Wang, X.; Gerdes, H.H. Transfer of mitochondria via tunneling nanotubes rescues apoptotic PC12 cells. *Cell Death Differ* **2015**, *22*, 1181-1191, doi:10.1038/cdd.2014.211.

100. Hase, K.; Kimura, S.; Takatsu, H.; Ohmae, M.; Kawano, S.; Kitamura, H.; Ito, M.; Watarai, H.; Hazelett, C.C.; Yeaman, C.; et al. M-Sec promotes membrane nanotube formation by interacting with Ral and the exocyst complex. *Nat Cell Biol* **2009**, *11*, 1427-1432, doi:10.1038/ncb1990.

101. Hanna, S.J.; McCoy-Simandle, K.; Leung, E.; Genna, A.; Condeelis, J.; Cox, D. Tunneling nanotubes, a novel mode of tumor cell-macrophage communication in tumor cell invasion. *J Cell Sci* **2019**, *132*, doi:10.1242/jcs.223321.

102. Lou, E.; Fujisawa, S.; Morozov, A.; Barlas, A.; Romin, Y.; Dogan, Y.; Gholami, S.; Moreira, A.L.; Manova-Todorova, K.; Moore, M.A. Tunneling nanotubes provide a unique conduit for intercellular transfer of cellular contents in human malignant pleural mesothelioma. *PLoS One* **2012**, *7*, e33093, doi:10.1371/journal.pone.0033093.

103. Lu, J.; Zheng, X.; Li, F.; Yu, Y.; Chen, Z.; Liu, Z.; Wang, Z.; Xu, H.; Yang, W. Tunneling nanotubes promote intercellular mitochondria transfer followed by increased invasiveness in bladder cancer cells. *Oncotarget* **2017**, *8*, 15539-15552, doi:10.18632/oncotarget.14695.

104. Pasquier, J.; Guerrouahen, B.S.; Al Thawadi, H.; Ghiabi, P.; Maleki, M.; Abu-Kaoud, N.; Jacob, A.; Mirshahi, M.; Galas, L.; Rafii, S.; et al. Preferential transfer of mitochondria from endothelial to cancer cells through tunneling nanotubes modulates chemoresistance. *J Transl Med* **2013**, *11*, 94, doi:10.1186/1479-5876-11-94.

105. Marlein, C.R.; Zaitseva, L.; Piddock, R.E.; Robinson, S.D.; Edwards, D.R.; Shafat, M.S.; Zhou, Z.; Lawes, M.; Bowles, K.M.; Rushworth, S.A. NADPH oxidase-2 derived superoxide drives mitochondrial transfer from bone marrow stromal cells to leukemic blasts. *Blood* **2017**, *130*, 1649-1660, doi:10.1182/blood-2017-03-772939.

106. Nakhle, J.; Khattar, K.; Ozkan, T.; Boughlita, A.; Abba Moussa, D.; Darlix, A.; Lorcy, F.; Rigau, V.; Bauchet, L.; Gerbal-Chaloin, S.; et al. Mitochondria Transfer from Mesenchymal Stem Cells Confers Chemoresistance to Glioblastoma Stem Cells through Metabolic Rewiring. *Cancer Res Commun* **2023**, *3*, 1041-1056, doi:10.1158/2767-9764.CRC-23-0144.

107. Saha, T.; Dash, C.; Jayabalan, R.; Khiste, S.; Kulkarni, A.; Kurmi, K.; Mondal, J.; Majumder, P.K.; Bardia, A.; Jang, H.L.; et al. Intercellular nanotubes mediate mitochondrial trafficking between cancer and immune cells. *Nat Nanotechnol* **2022**, *17*, 98-106, doi:10.1038/s41565-021-01000-4.

108. Resnik, N.; Baraga, D.; Glazar, P.; Jokhadar Zemljic, S.; Derganc, J.; Sepcic, K.; Veranic, P.; Kreft, M.E. Molecular, morphological and functional properties of tunnelling nanotubes between normal and cancer urothelial cells: New insights from the in vitro model mimicking the situation after surgical removal of the urothelial tumor. *Front Cell Dev Biol* **2022**, *10*, 934684, doi:10.3389/fcell.2022.934684.

109. Lokar, M.; Kabaso, D.; Resnik, N.; Sepcic, K.; Kralj-Iglic, V.; Veranic, P.; Zorec, R.; Iglic, A. The role of cholesterol-sphingomyelin membrane nanodomains in the stability of intercellular membrane nanotubes. *Int J Nanomedicine* **2012**, *7*, 1891-1902, doi:10.2147/IJN.S28723.

110. Gousset, K.; Gordon, A.; Kumar Kannan, S.; Tovar, J. A novel Microproteomic Approach Using Laser Capture Microdissection to Study Cellular Protrusions. *Int J Mol Sci* **2019**, *20*, doi:10.3390/ijms20051172.

111. Mehta, S.; Zhang, J. Liquid-liquid phase separation drives cellular function and dysfunction in cancer. *Nat Rev Cancer* **2022**, *22*, 239-252, doi:10.1038/s41568-022-00444-7.

112. Dubey, G.P.; Ben-Yehuda, S. Intercellular nanotubes mediate bacterial communication. *Cell* **2011**, *144*, 590-600, doi:10.1016/j.cell.2011.01.015.

113. Dubey, G.P.; Malli Mohan, G.B.; Dubrovsky, A.; Amen, T.; Tsipshtein, S.; Rouvinski, A.; Rosenberg, A.; Kaganovich, D.; Sherman, E.; Medalia, O.; et al. Architecture and Characteristics of Bacterial Nanotubes. *Dev Cell* **2016**, *36*, 453-461, doi:10.1016/j.devcel.2016.01.013.

114. Stempler, O.; Baidya, A.K.; Bhattacharya, S.; Malli Mohan, G.B.; Tzipilevich, E.; Sinai, L.; Mamou, G.; Ben-Yehuda, S. Interspecies nutrient extraction and toxin delivery between bacteria. *Nat Commun* **2017**, *8*, 315, doi:10.1038/s41467-017-00344-7.

115. Bhattacharya, S.; Baidya, A.K.; Pal, R.R.; Mamou, G.; Gatt, Y.E.; Margalit, H.; Rosenshine, I.; Ben-Yehuda, S. A Ubiquitous Platform for Bacterial Nanotube Biogenesis. *Cell Rep* **2019**, *27*, 334-342 e310, doi:10.1016/j.celrep.2019.02.055.

116. Zhang, J.; Wang, H.; Xie, T.; Huang, Q.; Xiong, X.; Liu, Q.; Wang, G. The YmdB protein regulates biofilm formation dependent on the repressor SinR in Bacillus cereus 0-9. *World J Microbiol Biotechnol* **2020**, *36*, 165, doi:10.1007/s11274-020-02933-z.

117. Kampf, J.; Gerwig, J.; Kruse, K.; Cleverley, R.; Dormeyer, M.; Grunberger, A.; Kohlheyer, D.; Commichau, F.M.; Lewis, R.J.; Stulke, J. Selective Pressure for Biofilm Formation in Bacillus subtilis: Differential Effect of Mutations in the Master Regulator SinR on Bistability. *mBio* **2018**, *9*, doi:10.1128/mBio.01464-18.

118. Pospisil, J.; Vitovska, D.; Kofronova, O.; Muchova, K.; Sanderova, H.; Hubalek, M.; Sikova, M.; Modrak, M.; Benada, O.; Barak, I.; et al. Bacterial nanotubes as a manifestation of cell death. *Nat Commun* **2020**, *11*, 4963, doi:10.1038/s41467-020-18800-2.

119. Fernandez-Calvino, L.; Faulkner, C.; Walshaw, J.; Saalbach, G.; Bayer, E.; Benitez-Alfonso, Y.; Maule, A. Arabidopsis plasmodesmal proteome. *PLoS One* **2011**, *6*, e18880, doi:10.1371/journal.pone.0018880.

120. Simpson, C.; Thomas, C.; Findlay, K.; Bayer, E.; Maule, A.J. An Arabidopsis GPI-anchor plasmodesmal neck protein with callose binding activity and potential to regulate cell-to-cell trafficking. *Plant Cell* **2009**, *21*, 581-594, doi:10.1105/tpc.108.060145.

121. Thomas, C.L.; Bayer, E.M.; Ritzenthaler, C.; Fernandez-Calvino, L.; Maule, A.J. Specific targeting of a plasmodesmal protein affecting cell-to-cell communication. *PLoS Biol* **2008**, *6*, e7, doi:10.1371/journal.pbio.0060007.

122. Moro, L. Snapshot on Cell-to-Cell Communication Nanotubes: From Bacteria to Humans. *Biology (Basel)* **2026**, *15*, doi:10.3390/biology15060513.

123. Lee, J.Y. New and old roles of plasmodesmata in immunity and parallels to tunneling nanotubes. *Plant Sci* **2014**, *221-222*, 13-20, doi:10.1016/j.plantsci.2014.01.006.

124. Bloemendal, S.; Kuck, U. Cell-to-cell communication in plants, animals, and fungi: a comparative review. *Naturwissenschaften* **2013**, *100*, 3-19, doi:10.1007/s00114-012-0988-z.

125. Baidya, A.K.; Rosenshine, I.; Ben-Yehuda, S. Donor-delivered cell wall hydrolases facilitate nanotube penetration into recipient bacteria. *Nat Commun* **2020**, *11*, 1938, doi:10.1038/s41467-020-15605-1.

126. Angulo-Canovas, E.; Bartual, A.; Lopez-Igual, R.; Luque, I.; Radzinski, N.P.; Shilova, I.; Anjur-Dietrich, M.; Garcia-Jurado, G.; Ubeda, B.; Gonzalez-Reyes, J.A.; et al. Direct interaction between marine cyanobacteria mediated by nanotubes. *Sci Adv* **2024**, *10*, eadj1539, doi:10.1126/sciadv.adj1539.

127. Sivabalasarma, S.; Wetzel, H.; Nussbaum, P.; van der Does, C.; Beeby, M.; Albers, S.V. Analysis of Cell-Cell Bridges in Haloferax volcanii Using Electron Cryo-Tomography Reveal a Continuous Cytoplasm and S-Layer. *Front Microbiol* **2020**, *11*, 612239, doi:10.3389/fmicb.2020.612239.

128. Brunkard, J.O.; Zambryski, P.C. Plasmodesmata enable multicellularity: new insights into their evolution, biogenesis, and functions in development and immunity. *Curr Opin Plant Biol* **2017**, *35*, 76-83, doi:10.1016/j.pbi.2016.11.007.

Supplementary Files

This is a list of supplementary files associated with this preprint. Click to download.

- SupplementaryMaterials.docx